Nanoparticle-Based Drug Delivery and the Impacts on Cancer Cell Biophysical Markers

Hesam Babahosseini

Thesis submitted to the faculty of the Virginia Polytechnic Institute and State University in partial fulfillment of the requirements for the degree of

Master of Science

In

Biological System Engineering

Chenming (Mike) Zhang, Chair

Masoud Agah, Co-Chair

Webster Santos

25th of September, 2015

Blacksburg, Virginia

Keywords: MicroElectroMechanical Systems (MEMS), Microfluidics, Biosensor, Nanoparticles, Drug Delivery, Biomechanics, Bioelectronics, Breast Cancer, MDA-MB-231, Sphingosine Kinase Inhibitors

Nanoparticle-Based Drug Delivery and the Impacts on Cancer Cell Biophysical Markers

Hesam Babahosseini

ABSTRACT

Cancer progression and physiological changes within the cells are accompanied by alterations in the biophysical properties. Therefore, the cell biophysical properties can serve as promising markers for cancer detection and physiological activities. To aid in the investigation of the biophysical markers of cells, a microfluidic chip has been developed which consists of a constriction channel and embedded microelectrodes. Single-cell impedance magnitudes at four frequencies and entry and travel times are measured simultaneously during their transit through the constriction channel. This microchip provides a high-throughput, label-free, automated assay to define biophysical signatures of malignant cells and monitor the therapeutic efficacy of drugs. Here, we monitored the dynamic cellular biophysical markers in response to sphingosine kinase inhibitors (SphKIs), and compared the effectiveness of drug delivery using Poly(lactic-co-glycolic acid) (PLGA) nanoparticles (NPs) loaded with SphKIs versus conventional delivery. Cells treated with SphKIs showed significantly higher impedance magnitudes at all four frequencies. The bioelectrical parameters extracted using a model also revealed that the highly aggressive breast cells treated with SphKIs shifted electrically towards that of a less malignant phenotype; SphKI-treated cells exhibited an increase in cell-channel interface resistance and a significant decrease in specific membrane capacitance. Furthermore, SphKI-treated cells became slightly more deformable as measured by a decrease in their channel entry and travel times. We observed no significant difference in the bioelectrical changes produced by SphKI delivered conventionally or with NPs. However, NPs-packaged delivery of SphKI decreased the cell deformability. In summary, the results showed that while the bioelectrical properties of the cells were dominantly affected by SphKIs, the biomechanical properties were mainly changed by the NPs.

This thesis is dedicated to my beloved wife, Hasti

and to my dearest parents, Ali and Fatemeh

Acknowledgments

In the Name of God, the Most Gracious, the Most Merciful,

Here, I would like to express my sincere gratitude to Dr. Mike Zhang, my advisor and head of my committee, who gave me the opportunity of earning my second MSc degree in the department of Biological System Engineering. Beside his outstanding scientific aspects, his impressive and respectful personality learned me a lot.

After that, I must extend my deepest thanks to Prof. Masoud Agah, my PhD advisor, who trusted me and generously allowed me to pursue a simultaneous degree along with my PhD study in the department of Mechanical Engineering.

Also, I must express my great appreciation to Dr. Webster Santos for serving in my committee, putting his valuable time and providing insightful ideas in our meetings.

Moreover, I owe my gratitude to Dr. Jeannine Strobl, Ms. Vaishnavi Srinivasaraghavan, Mr. Zongmin Zhao, Mr. Frank Gillam, and Ms. Elizabeth Childress who helped me to accomplish this thesis. Without their help, this thesis would not have been possible.

I would like to thank Dr. Kristi DeCourcy at the Fralin life science institute, Mrs. Kathy Lowe at the Morphology Service Laboratory in Vet Med, and Mr. Donald Leber at the Micro & Nano Fabrication Laboratory, all in Virginia Tech for equipment supports.

This project was financially supported by the National Science Foundation under award # CBET-1403304 and the National Institute of Health under award # U01DA036850.

Finally, I am extremely thankful to my wife, Hasti for her love and devotion, and especially her patience during accomplishment of this thesis. Last but not the least, I am heartily grateful to my dearest parent, because of them I am here right now.

Hesam Babahosseini, 9/11/2015, Blacksburg, VA

Table of Contents

List of Figures

1 Introduction

The biophysical properties of cells including their biomechanical and bioelectrical properties vary as a function of their tumorigenicity, metastatic potential, and health state. A more thorough understanding of cancer pathology, with possible gains in therapeutic insights, might be achieved through development of methods to monitor how cancer comes to dysregulate cell biophysical behaviors. Cancer pathology directly impacts and dysregulates cell biophysical behaviors through changes in cell membrane, cytoskeleton, and cytosol composition. The decrease in the cell stiffness and viscosity is a well-documented biomechanical signature during cancer progression which facilitates metastasis [1-3]. This change in the cell biomechanical properties is associated with the disorganization and decrease in concentration of the fundamental components of the cell cytoskeleton [4]. Furthermore, bioelectrical properties of cells are also altered during cancer progression because of the changes in cell membrane composition and internal conductivities [5, 6]. In this regard, cancer chemotherapeutic agents are purposely designed to target the cell structure, and consequently alter cell biophysical characteristics. The effects of drugs on biophysical properties of cells have been evaluated to provide insights into the sensitivity and efficiency of chemotherapies [7-11].

However, chemotherapy is often non-specific to cancer cells, which causes many severe toxic side-effects. In contrast to the conventional method of delivering medications, nanoparticles (NPs) offer approaches to drug-packaged delivery as a means to reduce off-target toxicity and enhance drug bioavailability by improving the timed release of drugs [12]. NPs are being used for targeted drug-delivery to cancer cells [13, 14]. It is notable that while the delivery of anti-cancer drugs to the specific cells can provide the desired chemotherapeutic effects, the side-effects of intracellular NPs are often unclearSeveral studies have analyzed the changes in the biomechanical properties of cells and their cytoskeleton architecture when exposed to NPs. For instance, the recent results indicate that the stiffness of mesenchymal stem cells increased under the impact of silica (Si) and silica-boron (SiB) NPs as a result of F-actin structural reorganization [15]. Moreover, hematite NP-treated *Escherichia coli* cells become significantly stiffer than untreated cells [16]. In addition, the super-paramagnetic iron oxide NPs increased cell elastic modulus of endothelial cells by 50% and formed actin stress fibers within the

cells [17]. However, there are some other studies with opposing results on cell biomechanics. For example, selenium (Se) NPs have been shown to remarkably decrease the Young's modulus of MCF-7 cells by disturbing membrane molecules and F-actin and inducing toxicity [18]. All these observations indicate that NPs have significant impact on cell biophysical attributes even if not loaded with drugs. The combinatory effects of NPs loaded with chemotherapeutic agents on cancer cells by means of the biophysical properties is untouched despite its significance.

This thesis aims to investigate the impact of new potential anti-cancer drugs [19], sphingosine kinase inhibitors (SphKIs), delivered by NPs on cancer cells utilizing a single cell-based assay. The significance of single-cell resolution assessment is further highlighted by considering that many biological experiments are carried out on cell populations ignoring the fact cancer masses are comprised of a heterogeneous mixture of cancer cells.

In this thesis, a high-throughput, label-free microfluidic chip is developed for screening biophysical (bioelectrical and biomechanical) properties of individual cells in heterogeneous cell populations. The uniquely designed microfluidic chip equipped with embedded parallel microelectrodes enables the deformation of single cells as they pass through a constriction and fully automated single-cell bioelectrical (multi-frequency impedance magnitudes) and biomechanical (entry and travel times) measurements. In this microchip, impedance is continuously monitored in real-time as cells transition between a mechanically non-disruptive channel into a narrow deformation region producing mechanical stress by deforming the cell membrane, cytoplasm, and nuclear structures, and as cells relax upon exiting the deformation region. This microchip is sensitive to alterations in cell biophysical markers and has application to detection of cellular responses to pharmaceutics.

To evaluate NP-mediated drug delivery, SphKIs were loaded into biodegradable poly(lactic-co-glycolic acid) (PLGA) NPs [20, 21]. Human MDA-MB-231 cancer cells representative of highly invasive breast cancer were exposed to SphKIs treatments, then introduced into the microfluidic device where biophysical measurements were captured and compared. Concurrent biological experiments and mathematical modeling were carried out as an approach to associate biophysical alterations with cell structural

components. The selective targeting of SphKIs to cancer cells using NPs coupled to determining cellular biophysical changes using a single-cell resolution microfluidic chip is novel. The approaches taken in this work can be applied to the analysis of NPs carrier-effects on the biophysical properties of cells as well as to drug screening and development of new cancer drugs to deter cancer progression by reversing aberrant biophysical properties.

2 Background

2.1 Nanoparticle-Based Drug Delivery

Delivering therapeutic compound to the target site is a major problem in treatment of different diseases. NP-based drug delivery provides several advantages comparing to the conventional forms of drug treatments. In NP-based drug delivery, a drug is packaged in NPs and transported to the target site, hence, its undesirable side-effects are minimized. Moreover, NP-based drug delivery leads to the improvement in the delivery of poorly water-soluble (hydrophobic) drugs, protection of the drugs from harsh environment, enhancement in drug bioavailability, improvement in the timed release of drugs, and reduction in the amount of consumed drug, and finally co-delivery of multiple types of drugs.

Cell-specific targeting can be accomplished by attaching drugs to specially designed carriers. A drug may be adsorbed, covalently attached or encapsulated into it. Cell-specific targeting may be accomplished by using active or passive strategies. The active mechanism relies on the attraction of the carriers to the target site by using the conjugation of receptor specific ligands. Once the drug-nanocarrier conjugates reach the target site, the therapeutic agents are released. For passive targeting, enhanced permeability and retention (EPR) effects help to spread the NPs inside the leaky cancer tissue and tumors or at the site of inflammation and infection [22]. A controlled release of drugs from nanocarriers can be achieved through changes in physiological environment such as pH, temperature, osmolality, or enzymatic activity.

Recent developments in nanotechnology have shown that NPs (structures smaller than 100 nm in at least one dimension) have a great potential as drug carriers. Various NPs, including liposomes, polymers, dendrimers, silicon or carbon materials, and magnetic NPs, are popular carriers in drug delivery. NPs used for medical applications have to be biocompaticle (able to integrate with a biological system without eliciting immune response) and nontoxic. Hydrodynamic size, shape, amount, surface chemistry, the route of administration, reaction of the immune system (especially a route of the uptake by macrophages and granulocytes) and residence time in the bloodstream are the factors which may affect the toxicity of NPs. For example for the hydrodynamic size, NPs with a hydrodynamic diameter of 10–100 nm have optimal pharmacokinetic properties for *in*

vivo applications. Smaller NPs are filtered out and cleared by the kidneys systems whereas larger ones are quickly removed from the bloodstream via the macrophages of the reticuloendothelial system [23]. Although complete clearance is eventually desired when the treatment is completed, the NPs must be able to avoid rapid clearance in order to achieve the desired targeting efficiency. In general, the circulation half-life of NPs should be prolonged to allow them to pass by a target site multiple times, giving them increased opportunities to accumulate at the target site [24].

The application of biodegradable nanosystems for the development of nanomedicines is one of the most successful ideas. Nanocarriers composed of biodegradable polymers undergo hydrolysis in the body, producing biodegradable metabolite monomers, such as lactic acid and glycolic acid. Kumari et al. [25] reported a minimal systemic toxicity associated with using of PLGA for drug delivery or biomaterial applications. Such NPs are biocompatible with tissue and cells [26]. Drug-biodegradable polymeric nanocarrier conjugates used for drug delivery are stable in blood, non-toxic, and non-thrombogenic. They are also non-immunogenic as well as non-proinflammatory, and they neither activate neutrophils nor affect reticuloendothelial system [27].

Whenever a NP encounters a cell, it must first cross the plasma membrane of a cell to be quickly internalized into the cells through endocytosis, an energy-dependent process defined as the internalization of cargo into a cell by engulfment. After internalization, the NPs enveloped by vesicles will be transported along the endolysosomal network to other organelles including endosomes, lysosomes, Golgi apparatus, mitochondria, endoplasmic reticulum (ER), and nucleus or sometimes even be exocytosed (excretion from the cell). As shown in Figure 2.1 [28], the intracellular trafficking of NPs is a very complex process that involves motor proteins shuttling the NP-loaded vesicles along cytoskeletal structures within a cell. For successful delivery of therapeutic agents, the NPs also need to escape from the endolysosomal network and enter the cytosol, where is the typical working site for most drugs. During the intracellular transport process, the NP has to be degraded or disassembled to allow for quick release of its payload.

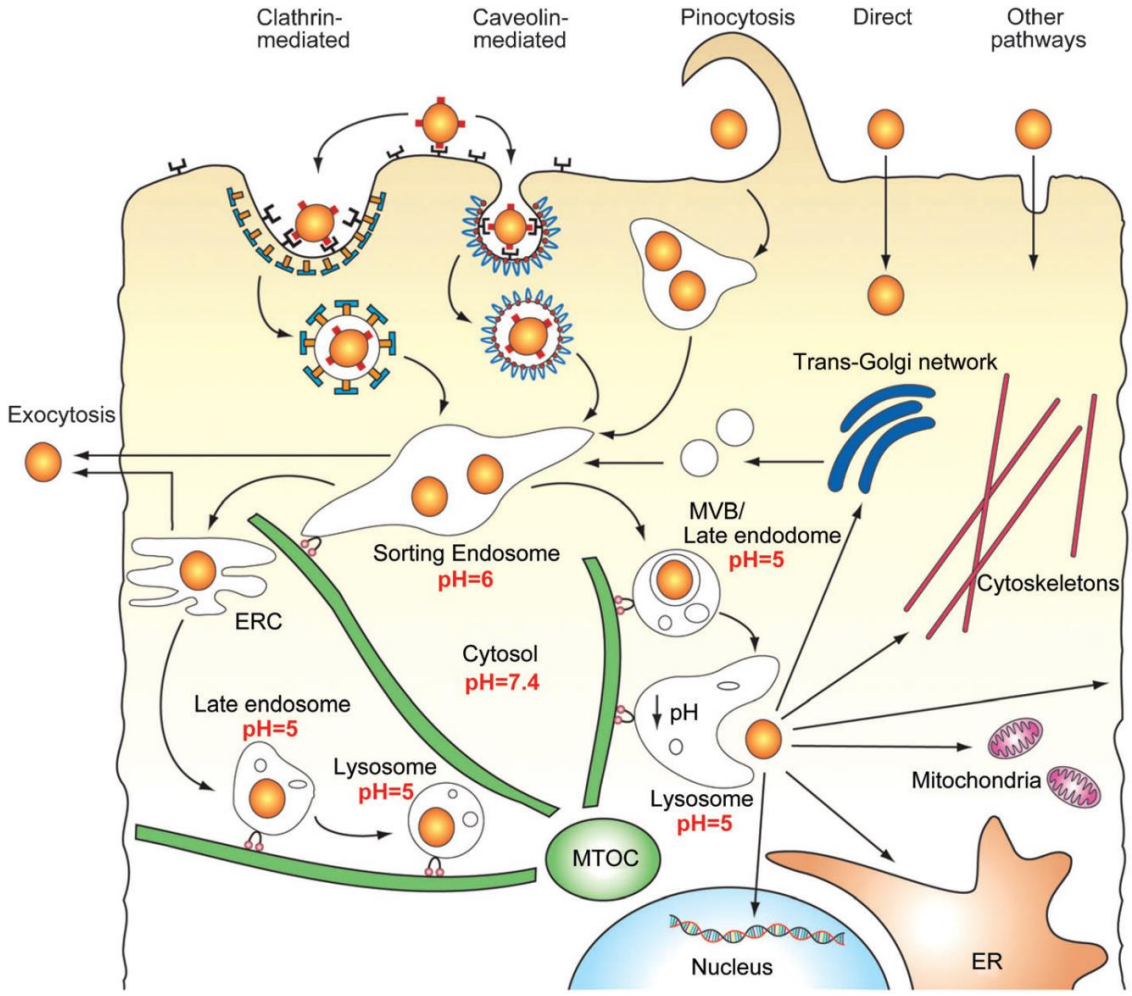

Figure 2.1 Intracellular transport of nanoparticles. After internalization, the nanoparticle is trafficked along the endolysosomal network in vesicles with the aid of motor proteins and cytoskeletal structures. Note the difference in pH values between different intracellular compartments. ER, endoplastic reticulum; ERC, endocytic recycling compartment; MTOC, microtubule-organizing center; MVB, multivesicular bodies [28]. T. Sun, Y. S. Zhang, B. Pang, D. C. Hyun, M. Yang, Y. Xia. Engineered Nanoparticles for Drug Delivery in Cancer Therapy. Angewandte Chemie International Edition. 2014;53:12320-64. Used under fair use, 2015.

The therapeutic applications of NPs are diverse, ranging from cancer therapeutics, antimicrobial actions, vaccine delivery, gene delivery and site-specific targeting to avoid the undesirable side effects of the current therapeutics. Many chemotherapeutic drugs such as carboplatin, paclitaxel, doxorubicin and etoposide, etc., have been successfully loaded onto NPs and these nanoparticulate systems are very potent against various cancers as demonstrated by the studies of various research groups. For example, PLGA NPs loaded with paclitaxel have found to be effective in chemotherapeutic of various

cancer cells [29]. Greater and sustained antiproliferative activity of paclitaxel-loaded PLGA NPs in HeLa cells was reported by Yang et al [30]. Enhanced apoptosis of HeLa cells was observed, which may be due to the sustained release of paclitaxel from the PLGA NPs, which in turn showed that PLGA NP-encapsulated paclitaxel is promising as a controlled drug-delivery system in future clinic application [30]. Paclitaxel-loaded Cetyl alcohol/polysorbate NPs have been shown higher brain and tumor cell uptake, thus leading to greater cytotoxicity [31]. Also, Polyisohexylcyanoacrylate (PIHCA) NPs with doxorubicin encapsulant have higher antitumor efficacy than native doxorubicin for hepatocellular carcinoma cells *in vitro* and *in vivo* and can overcome multiple drug resistance phenotype [32].

Although this is a relatively new field, various formulations are in clinical trials or have been successfully marketed. For example PEGylated liposome Doxil NPs for ovarian cancer and multiple myeloma (Janssen, Beerse, Belgium) with specific advantages such as enhanced circulation time and up to six times more effectiveness than free drug are now commercially available. Also, Albumin Abraxane NPs (Celgene, Summit, NJ) targeting lung and breast cancers with the advantages of increasing cytotoxicity while decreasing infusion time and required dose are now on market.

Understanding the *in vitro* delivery of NPs is a critical initial step toward their successful applications. On one hand, the NPs to serve as a drug carrier must be first evaluated *in vitro* at the cellular level before they are further tested *in vivo* at the tissue, organ, and body levels. On the other hand, only with sufficient knowledge of NP-cell interactions, one can start to engineer the properties of NPs for optimal delivery *in vivo* and effective cancer therapy.

2.2 Cell Biomechanical Properties

The study of cell mechanics has gained great significance in the past decades because mechanical loading of cells induces deformation and remodeling, which influence many aspects of a living cell. The collective mechanical interactions of multiple filamentous proteins in the cell cytoskeleton are responsible for the mechanical behavior [33]. The cell cytoskeleton not only provides mechanical support to the cell [34] but has been shown to play a pivotal role in transducing mechanical stimuli in the

microenvironment into intracellular signaling events and changes in gene expression [35], regulating differentiation [36], adhesion [37, 38], contractility, migration [39, 40] and other processes. These are mechanically-oriented processes that are of critical importance in developmental biology [41], tissue homeostasis and processes such as wound healing [42], but also contribute to diseases such as cancer [43]. The progression of cancer is associated with an alteration of the cytoskeleton [44]: metastatic cancer cells become softer to facilitate motility [45, 46]. In fact, aggressive cancer cells have acquired the ability to deform and squeeze through tissue matrix and access the circulatory systems and subsequently adhere to and extravasate blood or lymph vessels to establish secondary tumors [47, 48] suggesting that the metastatic potential of cancer cells is related to their mechanical properties. Furthermore, critical signaling intermediates are intracellular signaling pathways are altered due to the deregulation of cytoskeleton organization [49]. Therefore, the ability to characterize the mechanical nature of a cell could provide insight into how cells receive and integrate regulatory signals from the surrounding environment and the impact on normal development and disease progression.

A variety of methods have been developed to interrogate cellular mechanical properties, such as viscoelasticity and deformability, mainly at the single cell level [50-54]. The parameters typically used to describe the mechanical properties are the elastic modulus, which relates applied stresses and cell deformation [55, 56] and the viscosity modulus, which corresponds cell time-dependency stress relaxation response to a step displacement [57, 58]. To date, several experimental techniques have been developed to probe and quantify cell deformation characteristics, namely micropipette aspiration [59], parallel microplate devices [60], magnetic cytometry [61, 62], optical tweezers [63], optical stretching rheometry [64], and atomic force microscopy (AFM) [65, 66]. In general, cell biomechanical measurements using the different methods are in agreement that transformed cancerous cells are softer, more deformable, and less viscous than their healthier counterparts by means of measuring their elastic modulus [67] viscoelastic properties [68, 69].

In the previous studies, our group attempted to investigate the biomechanical responses of cancer cells via AFM [70]. First, Nikkhah et al. showed that MDA-MB-231 human

breast epithelia metastatic cells are significantly softer with on average a smaller elastic modulus comparing to MCF10A non-invasive cells [71]. Their findings on 3D microstructures also demonstrated that while cancer cells deform to take the shape of the curved sidewalls in microengineered wells, normal cells stretch their cytoskeleton to avoid them [72, 73]. Using AFM analyses, they showed later that the growth media composition has a pronounced effect on cells elasticity [74]. In 2012, Ketene et al. investigated the mechanical responses of mouse ovarian surface epithelial (MOSE) cells, a developed mouse cell line that can represent the early, intermediate, and late stages of human ovarian cancer [4]. With the use of AFM, they showed the results pertaining to the rate of change in cell viscoelasticity during the gradual progression of cancer disease [4]. Another study on MOSE cells by them was devoted to cytoskeleton component analysis in the determination of their exact roles in the cell's mechanical behavior [75]. The results introduced actin filaments as the primary player in structural integrity and viscoelastic responses in cells. In 2013, Babahosseini et al. determined the differential effects of exogenous sphingolipid metabolites on the elastic modulus of mouse ovarian surface epithelial cells as they transition to cancer [76]. Later in 2014, our group showed that the elastic properties of cancer stem-like/tumor initiating cells enriched from ovarian cancer cells exhibit considerably softer and more homogeneous characteristics in comparison to their less aggressive counterparts [1]. Recently, we showed that the living cells exactly exhibit a fractional power-law viscoelastic response instead of a simple exponentially decaying function, commonly used for viscoelastic behavior of the living cells [2]. We also used AFM for biomechanical characterization of the sub-cellular layers in single normal and cancer cells [3]. So far, the static single force has been typically used to characterize the cell biomechanical properties which is insufficient to explain the biomechanical responses of cells in dynamically changing physiological conditions. Our group has very recently produced solid evidence using indicating that cancer cells at different disease stages can respond differently to cyclic forces applied to them via AFM which resemble dynamic *in vivo* microenvironment [77]. Advanced metastatic cancer cells show "softening" behavior while benign cells stiffen. We used this distinct different responses to differentiate normal and cancer cells with a confidence level as high as 95%.

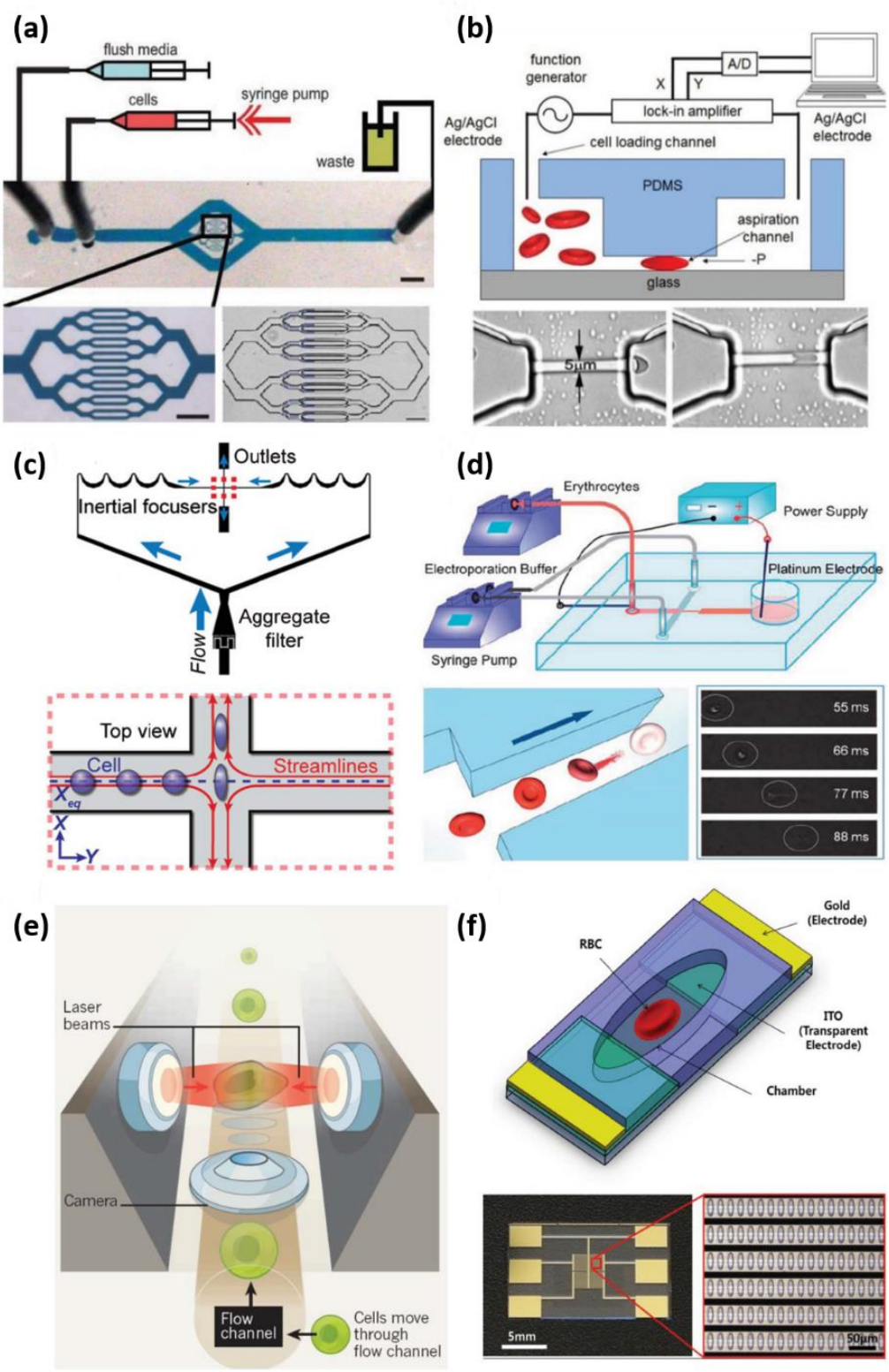

Figure 2.2 (a) A microfluidic biophysical flow cytometer device including a network of 64 parallel capillary-like microchannels for blood cell deformability measurement using a high speed camera [78]. M. J. Rosenbluth, W. A. Lam, D. A. Fletcher. Analyzing cell mechanics in hematologic diseases with microfluidic biophysical flow cytometry. Lab Chip. 2008;8:1062-70. Used under fair use, 2015.

(b) A microfluidic system for characterizing the bioelectrical and biomechanical properties of RBCs at 100–150 cells/s. The transit time measurements are made using electrical impedance changes when an RBC passes through the constriction channel [79]. Y. Zheng, E. Shojaei-Baghini, A. Azad, C. Wang, Y. Sun. High-throughput biophysical measurement of human red blood cells. Lab Chip. 2012;12:2560-7. Used under fair use, 2015. (c) Hydrodynamic stretching microfluidic cytometry device that focuses cells to the center lines of the test channel by inertial effects and then stretches them by fluid pressure and finally analyzes their deformability by high-speed imaging at a high-throughput of 2,000 cells/s [80]. D. R. Gossett, H. T. K. Tse, S. A. Lee, Y. Ying, A. G. Lindgren, O. O. Yang, et al. Hydrodynamic stretching of single cells for large population mechanical phenotyping. Proc Natl Acad Sci USA. 2012;109:7630-5. Used under fair use, 2015. (d) An electroporation-induced microfluidic device for lysing RBCs at the single cell level in the narrow section by applying a constant DC voltage. RBCs lysis time obtained by high-speed time-lapse imaging is correlated to their deformability [81]. N. Bao, G. C. Kodippili, K. M. Giger, V. M. Fowler, P. S. Low, C. Lu. Single-cell electrical lysis of erythrocytes detects deficiencies in the cytoskeletal protein network. Lab Chip. 2011;11:3053-6. Used under fair use, 2015. (e) An optical stretcher uses two laser beams to trap and deform cells travelling along a flow channel. The cell deformation images are recorded and analyzed to assess their elasticity and contractility [82]. E. Jonietz. Mechanics: The forces of cancer. Nature. 2012;491:S56-S7. Used under fair use, 2015. (f) A microchamber array integrated with electrodes for electro-deformation of individual trapped RBCs by applying a DEP force [83]. I. Doh, W. C. Lee, Y. H. Cho, A. P. Pisano, F. A. Kuypers. Deformation measurement of individual cells in large populations using a single-cell microchamber array chip. Appl Phys Lett. 2012;100:173702. Used under fair use, 2015.

By the way, AFM and other techniques suitable for single-cell analysis such as micropipette aspiration, optical tweezers, and magnetic tweezers have extremely low throughput (1cell per 2-10min). The emerging need for a high-throughput clinically relevant alternative technique for evaluating deformability of individual cell has led to the development of microfluidic-based analyzers [84]. Microfluidic-based analyzers are high-throughput tools (up to 1000 cells per 1min) for determining biophysical signatures at single-cell resolution. For characterizing the biomechanical properties of a cell, the cell must be deformed. Thus, microfluidic-based analyzers for cell deformability measurements can be classified based on the mechanical stimuli applied to deform the cell [84] into structure-induced deformation (e.g. Figure 2.2.a [78] and Figure 2.2.b [79]), fluid-induced deformation (e.g. Figure 2.2.c [80], electroporation-induced deformation (e.g. Figure 2.2.d [81]), optical stretcher (e.g. Figure 2.2.e [82]), and dielectrophoresis (DEP)-induced deformation (e.g. Figure 2.2.f [83]). In structure-induced deformation microfluidic-based analyzer category where the microchip developed in this thesis falls, single cells move through a constriction channel that imposes mechanical stress on the cell body, and the transit time is measured using image data or electrical resistance

changes which provides rapid and fully automated acquisition of the cell deformability biomarker [78-80, 85-87]. The results from these analyzers show that the average transit time of cancer cells is significantly shorter than that of normal cells. With considering this fact that the transit time is directly correlated with cell deformability, the results match the earlier reports generated by the traditional tools like AFM.

2.3 Cell Bioelectrical Properties

Besides mechanical properties, electrical properties of cells are also important biophysical properties. The electrical properties of biological cells can also be altered in the progression of cancer. These alterations are because of the changes in the dielectric properties of cells which are governed by cell membrane composition and morphology, internal conductivities, and size [88, 89]. Generally, the electrical properties of a membrane are affected by the membrane morphology, lipid bilayer composition and thickness, and embedded proteins [90-92]. Electrical properties of the cytoplasm are influenced by the intracellular structures and physiological conditions (e.g., nucleus-to-cytoplasm ratio and ion concentrations inside the cell) [93-95].

The electrical properties of biological samples can be assessed through bioimpedance measurements on adherent or suspended cells. Single cell bioimpedance has gained broad acceptance in cancer research to discriminate normal and malignant cell types [96-98]. In addition, bioimpedance analyses show promise as a means to assess anti-cancer, anti-proliferative, or apoptosis-induced drugs [99, 100]. Han et al. have conducted single cell analysis of breast cancer cell lines including non-tumorigenic MCF10A, benign MDA-7, and metastatic MDA-MB-231 and MDA-MB-435 to extract the differences in magnitude and phase of measured impedance over the frequency range of 100 Hz to 3 MHz and membrane capacitance and resistance at 100 kHz among these cell lines [101]. Qiao et al. reported differences in the impedance of MDA-MB-231 and MCF10A breast cells in suspension [102]. Hong et al. measured the differences in the biomedicine of MDA-MB-231 and MCF-7 cells using a microfluidic device that traps single cells using DEP forces [103]. Srinivasaraghavan et al. in our VT MEMS group actively work on the development of impedance biosensor microchips for cancer research and used them to measure the bioimpedance of different breast cancer cell lines [104-

106]. All these studies demonstrate the potential of analyzing the bioelectrical heterogeneity of cell populations and using them as possible label-free biomarkers to predict the progression of cancer, its metastatic potential, and its response to drug treatments.

The ease and versatility of bioimpedance measurements, rich-content information offered by bioimpedance spectroscopy provides promise for development of low-cost, label-free, and high-throughput bioimpedance sensing platforms for cell analyses and cancer diagnosis and prognosis. Moreover, more recent improvements in microengineering have made the integration of electrodes with microelectromechanical systems (MEMS) and microfluidic devices for miniaturization of bioelectrical sensing platforms to be feasible.

Microfluidic devices for single-cell electrical measurement can be categorized [84, 107] into microfluidic patch-clamping (e.g. Figure 2.3.a [108]), impedance flow cytometry (e.g. Figure 2.3.b [109]), electrorotation (e.g. Figure 2.3.c [110]), and microfluidic electrical impedance spectroscopy (e.g. Figure 2.3.d [111]). The microchip developed in this thesis falls in the impedance flow cytometry category. In the developed microchip, the bioimpedance of single cells tightly moving through a constriction channel is measured and that minimizes the undesirable leakage current commonly happening in the impedance flow cytometry.

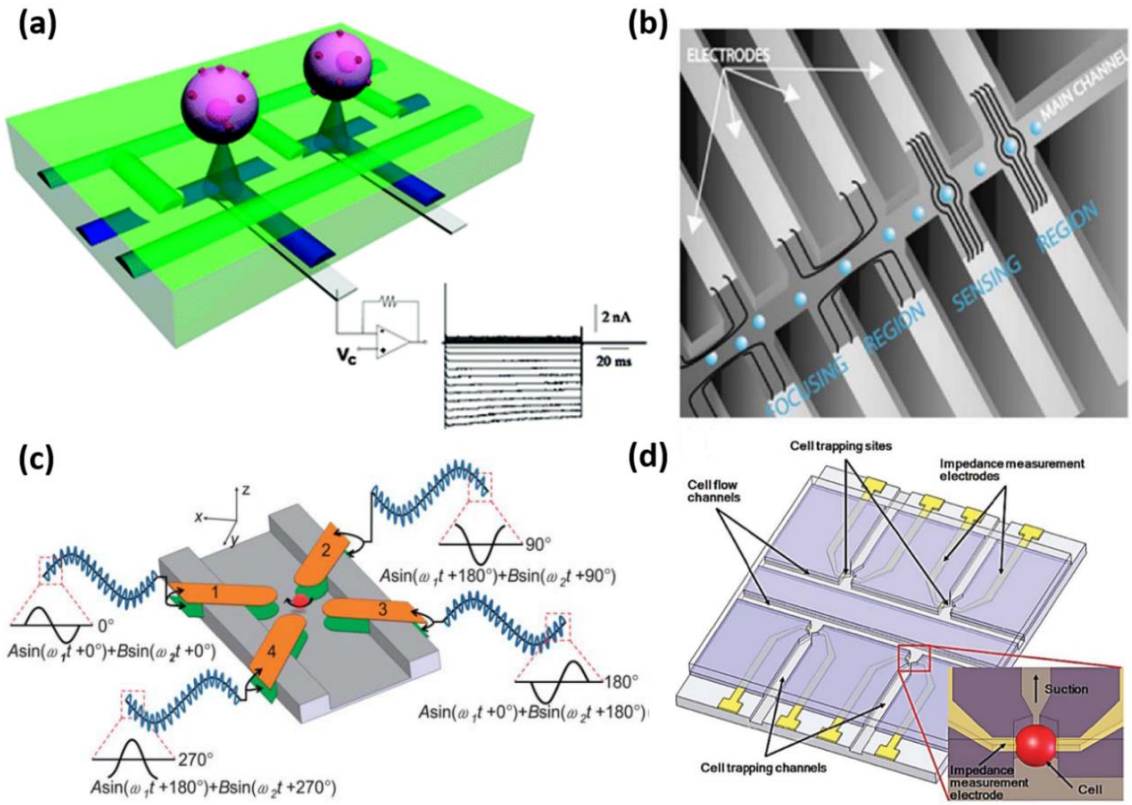

Figure 2.3 (a) A microfluidic patch-clamping system having a 2 µm air-blown aperture for trapping and measuring single cell ionic currents flowing through a cell's plasma membrane [108]. X. Li, K. G. Klemic, M .A. Reed, F. J. Sigworth. Microfluidic System for Planar Patch Clamp Electrode Arrays. Nano Lett. 2006;6:815-9. Used under fair use, 2015. (b) An impedance flow cytometer chip merging DEP focusing and impedance sensing [109]. G. Mernier, E. Duqi, P. Renaud. Characterization of a novel impedance cytometer design and its integration with lateral focusing by dielectrophoresis. Lab Chip. 2012;12:4344-9. Used under fair use, 2015. (c) An electrorotation (ROT)-microchip including four micro-electrodes connected for trapping and simultaneously rotating of single cells by DEP forces which allows cellular biophysics measurements using rotation spectra (rotation rate vs. frequency) [110]. S. I. Han, Y. D. Joo, K. H. Han. An electrorotation technique for measuring the dielectric properties of cells with simultaneous use of negative quadrupolar dielectrophoresis and electrorotation. Analyst. 2013;138:1529-37. Used under fair use, 2015. (d) A microfluidic electrical impedance spectroscopy system containing four impedance analysis single-cell trap sites where a tight seal is formed between the cell and two integrated electrodes for impedance measurements [111]. Y. Cho, H. S. Kim, A. B. Frazier, Z. G. Chen, D. M. Shin, A. Han. Whole-Cell Impedance Analysis for Highly and Poorly Metastatic Cancer Cells. J. Microelectromech. 2009;18:808-17. Used under fair use, 2015.

2.4 Outline

Chapter 1 includes an introduction to this thesis.

Chapter 2 covers the backgrounds of concepts in this thesis. It includes the nanoparticle-based drug delivery especially in cancer therapy, and also cell biomechanical properties and cell bioelectrical properties.

Chapter 3 reports the design, fabrication and data acquisition process for the biosensor microchip. Briefly, the microchip is designed as an automated, high-throughput, single-cell-resolution assay for electromechanical characterization and profiling. The microchip is composed of PDMS and electrode layers which are fabricated by simple, low-cost soft-lithography and metallization techniques in cleanroom. The data acquisition is accomplished using the integrated electrodes at four frequencies in real time for both cell bioelectrical and biomechanical properties, simultaneously.

Chapter 4 includes the materials and methods used in this thesis. It includes the cell samples, the biological experiments, the drugs, the NPs and statistical analysis, used or performed in this thesis. The biological experiments are such as western blot analysis, immunofluorescence imaging, and transmission electron microscopy (TEM) imaging. The drugs are sphingosine kinase inhibitors which have potential as anticancer agents. Later, the process of fabrication and characterization of the PLGA polymeric NPs are explained.

Chapter 5 presents the results and discussions in two general sections of cell bioelectrical characterization and cell biomechanical characterization. In the first section, the cell bioimpedance data measured are presented at four frequencies and then an electric circuit model is fitted to the data to extract cell bioelectrical parameters. In the second section, cell deformability are graphed by entry and travel times indices and then cell cytoskeleton content is evaluated to provide supports for the measured cell deformability changes.

Finally, chapter 6 concludes this thesis and proposes ideas and suggestions for the future works.

3 Biosensor Microchip

3.1 Design

A microfluidic chip was designed and fabricated for high-throughput biophysical profiling of single cells. The operation of the microchip is shown schematically in Figure 3.1. The two principal parts of the microchip are the constriction and the delivery channels that deliver, trap, and pass the cells continuously as shown in Figure 3.2.A.

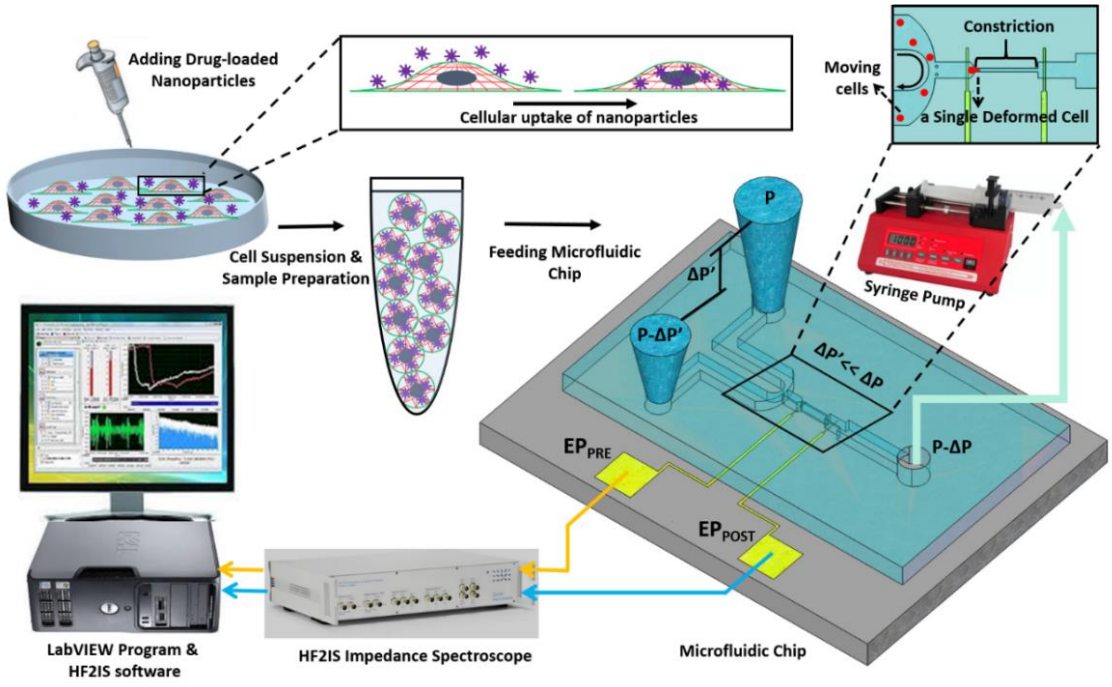

Figure 3.1 Schematic image showing the operation of the microfluidic chip.

The U-shaped delivery channel is a mechanism to deliver single cells at the entrance of the constriction channel to prevent clogging. A continuous free flow of undeformed suspended cells in culture medium is established in the delivery channel between the inlet/outlet by a difference in the level of solution in the reservoirs. The constriction channel dimensions are designed to be narrow (8µm-wide), shallow (8 µm-deep), and straight (100 µm-long) to enable deformation of cells as they are pulled through the constriction microchannel. Single cells are trapped and pulled continuously through the constriction channel as a result of constant pressure of -150 Pa imposed by a syringe pump (Harvard Apparatus, Holliston, MA) connected to another end of the constriction channel. Once a cell is trapped and is traveling through the microchannel, it completely blocks the

constriction channel so that another cell never enters. A parallel microelectrode pair is integrated on either side of the constriction channel for simultaneous measurements of the impedance at multiple frequencies and entry and transit times of single cells automatically as they pass through the constriction channel.

3.2 Fabrication

The microchip was obtained by casting polydimethylsiloxane (PDMS) on a two-layer SU-8 (MicroChem Corp., Westborough, MA) master fabricated using standard soft lithography techniques. Two layers of SU-8 on a silicon wafer are to obtain the shallow constriction channel (8 μm) and the deep delivery channel (30 μm) as shown in Figure 3.2.A. The process flow for fabrication of the microchip is shown in Figure 3.2.B. Briefly, the first layer of SU-8 (8 μm thick, SU-8 2007) was made to form the constriction channel, which was spun on the wafer, soft-baked, and exposed to ultraviolet (UV) light through the first chrome-on-glass mask. The wafer was then baked on a hot plate to cross-link the exposed SU-8. The second layer of SU-8 was made to form the delivery channel, which (22 μm thick, SU-8 2025) was spin-coated on the wafer, soft-baked, aligned, and then exposed to UV light through the second film mask, followed by post-exposure bake. Finally, the two-layer SU-8 was developed and hard baked.

PDMS pre-polymer was mixed with the curing agent at 10:1 ratio and molded onto the SU-8 master placed in an aluminum foil plate. The wafer was then placed in a vacuum desiccator to degas air bubbles in the PDMS before curing on a hot plate. The PDMS device was allowed to cool and then was peeled from the SU-8 master and diced. Inlet/outlet holes and suction port were punched into the PDMS.

To fabricate the electrode layer, photoresist AZ9260 was first spun coated on the Pyrex/glass wafer. After exposure through a mask and development in AZ400k, the electrode pattern was transferred onto the Pyrex/glass wafer. Then, a 25 nm and 100 nm layer of Cr and Au was deposited on the wafer by evaporation (PVD, Kurt J. Lesker, USA), respectively. Following by a lift-off process in acetone, the electrodes were patterned in the areas that were unprotected by the photoresist. The Pyrex wafer was then diced using the MA-1006 dicing saw to yield individual electrode chips.

For bonding, the diced electrode chip and the PDMS layer were concurrently treated with oxygen plasma in a plasma cleaner (Harrick Plasma, Plasma Cleaner) for 50 s per piece. A few drops of methanol were pipetted onto the electrode chip and the PDMS layer was aligned with the electrode layer under a microscope and pressed together to obtain the device.

3.3 Data Acquisition

The microchip was mounted on a general purpose board (GPB) with subminiature version A (SMA) adaptors. The HF2IS impedance spectroscope (Zurich instruments, Zurich, Switzerland) was used for continuous impedance measurements as a measure of the opposition to the flow of electric current. The impedances were measured at four frequencies of 1 kHz, 10 kHz, 100 kHz and 1 MHz in parallel using an excitation voltage of 2.25 V at each frequency. The Redlake NX-3 high speed camera (IDT, Pasadena, CA) was used to monitor and image the cells at the rate of 500 fps. Figure 3.2.C shows tracking of a cell in the captured images as it passes through the constriction channel. Figure 3.2.D shows the characteristic impedance profile at 1 kHz, which corresponds to the impedance changes recorded as the single cell moves through the constriction channel. The impedance magnitude measured from the culture medium alone is the baseline value. When a cell approaches the entrance of the constriction channel (Figure 3.2.C-a), the impedance increases with a steep slope. As the cell is trapped and squeezed into the constriction channel (Figure 3.2.C-b), the impedance magnitude rises gradually. The time the cell takes to deform and squeeze into the constriction channel is called the entry time. When the cell completely enters and travels the microchannel, the impedance magnitude suddenly rises and reaches a peak value (Figure 3.2.C-c). The cell exits the constriction channel rapidly as can be seen from the steep slope back to the baseline (Figure 3.2.C-d). The time the cell spends traveling through the constriction channel is called the travel time. Therefore, the entry and travel times of the cell through the constriction microchannel can be calculated from the impedance profile [112]. The impedance change between the peak and the baseline for single cells was calculated using real and imaginary parts of their complex impedance values.

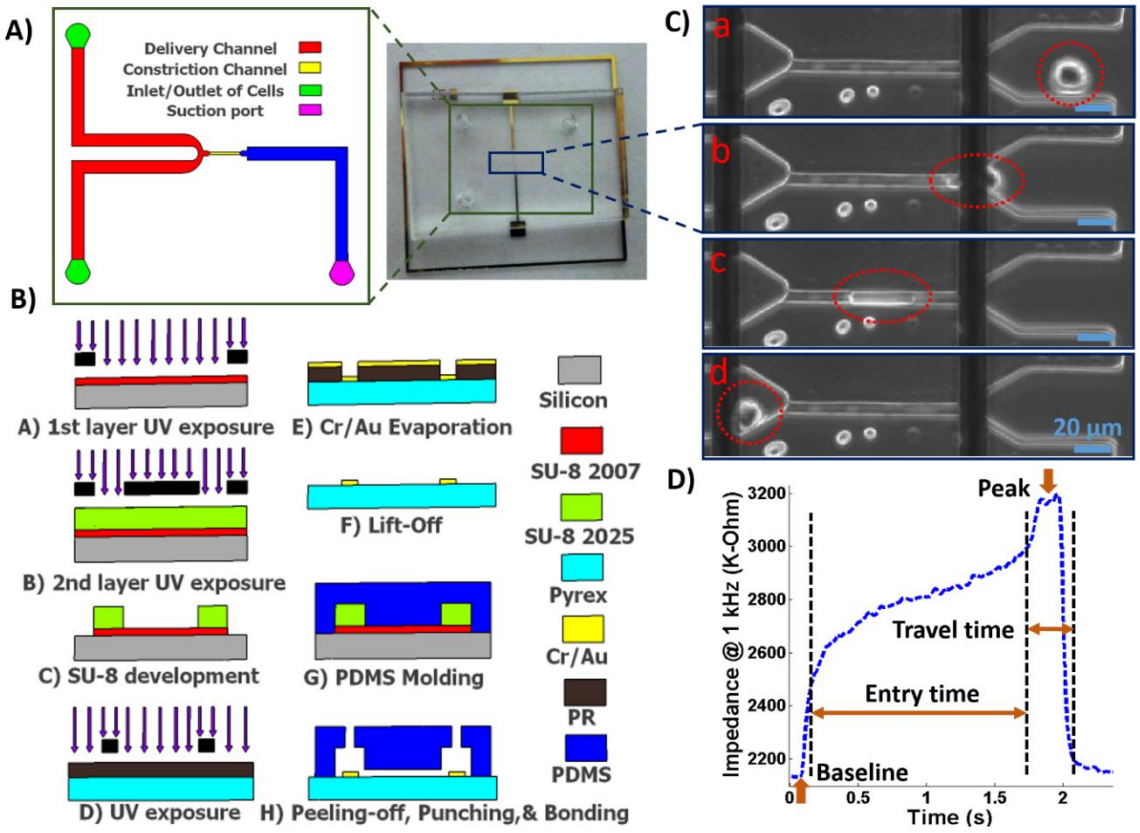

Figure 3.2 A) Illustration of the fabricated microfluidic chip including delivery and constriction channels, cells inlet/outlet, and suction port. B) Process flow for fabrication of the microfluidic device. C) Image showing a single deformed cell travelling through the constriction channel. D) The impedance magnitude change at 1 kHz when a single cell passes through the constriction channel.

4 Methods and Materials

4.1 Sample Preparation

MDA-MB-231 human epithelial breast cancer cell line (ATCC; American Type Culture Collection, Manassas, VA) representing highly invasive breast carcinoma was chosen in this study. MDA-MB-231 cells were grown in Dulbecco's modified Eagle's medium (DMEM) (ATCC, Manassas, VA) containing 10% fetal bovine serum (Atlanta Biologicals, Norcross, GA), penicillin-streptomycin (100 Units/mL), and 4 mM L-glutamine. The cells were grown in T-25 cm^2 culture flasks at 37 °C in humidified 5% CO_2-95% air atmosphere. For free-drug treatment of cancer cells with the SphKIs, each compound was added to the cell culture medium at a non-toxic concentration of 10 µM for the specified times indicated in the results section. For NP-packaged treatment of cancer cells, the PLGA NPs were introduced into the cell culture medium at a 10 µM final concentration of each SphKI loaded in NPs for the specified periods. To prepare samples for the microfluidic experiments, the cells were harvested and suspended in culture medium ($5x10^5$ cells/mL) and introduced into the microfluidic chip.

4.2 Biological Experiments

4.2.1 Western Blot Analysis

To quantify the relative content of actin proteins before and after treatments, Western blot (WB) analysis was performed. The cells were cultured to 70% confluency in a culture flask, and then harvested in a modified radio immunoprecipitation assay (RIPA) buffer (10 mM Tris-HCl, 1 mM EDTA, 1% Triton X-100, 0.1% sodium deoxycholate, 0.1% SDS, 140 mM NaCl) to obtain a whole-cell lysate. Samples were loaded onto a 4 -12% SDS PAGE gel for electrophoresis. A WB was performed with a Biorad Transblot Turbo system (Bio-Rad Laboratories Inc., Hercules, CA). Blocking of the membrane was done with a mixture of Tween Tris buffered saline (TTBS) buffer containing 5% nonfat dry milk. After two washes, the membrane was incubated with primary antibody solution containing a 1:2,000 dilution of mouse anti-actin (Sigma Aldrich, St. Louis, MO) in blocking buffer. Two washes in TTBS were performed and the membrane was incubated with a secondary antibody solution containing a 1:2,000

dilution of goat anti-mouse IgG antibody (Sigma Aldrich, St. Louis, MO) coupled to horseradish peroxidase (HRP). Chemiluminescence with Biorad Clarity substrate (Bio-Rad Laboratories Inc., Hercules, CA) was used to detect the presence of antibodies. Densitometry was performed using Biorad Image Lab software. Three biological replicates performed and the results showed as mean ± standard deviation ($P<0.01$).

4.2.2 Immunofluorescence Imaging

For confocal microscopy, cells were grown on culture plates for 24 hr before treatments; 48 hr after treatments, the cells were washed in Hank's balanced salt solution (HBSS), fixed with 3% paraformaldehyde (PF) in 250mM Tris, pH 7.2 for 10 minutes followed by 6% PF- 0.25% Triton X-100 in PBS for 10 minutes. The PLGA NPs were fluorescently labeled in their synthesis process by adding 0.2 mg/mL Nile red. For actin cytoskeleton staining, the cells were incubated with Alexa Fluor-488 phalloidin (Invitrogen, Carlsbad, CA) at room temperature (5 U/mL in 140 mM NaCl-6% bovine serum albumin in 40 mM Tris, pH 7.2, Invitrogen) for 15 minutes. Then, the samples were rinsed three times in PBS and mounted on ProLong Gold antifade reagent with DAPI (Invitrogen, Carlsbad, CA) to stain the cell nuclei. The confocal imaging was performed on the samples using a confocal laser scanning microscope (LSM510, Zeiss, Thornwood, NY). Actin content intensity was obtained from at least three fluorescence staining images using ImageJ software and the results showed as mean ± standard deviation ($P<0.01$).

4.2.3 TEM Imaging

Transmission electron microscopy (TEM) was performed to investigate the distribution of the NPs in the cells. For TEM imaging, the cells were grown on culture plates for 24 hr before adding the NPs. After 24 hr incubation, the culture medium was removed and the cells were washed 2 times with 0.1 M Na-Cacodylate for 15 minutes, and then post-fixed with 1% OsO_4 in 0.1 M Na-Cacodylate buffer, pH 7.2 for at least 1 hr. The buffer was removed and the cells were washed 2 times again in 0.1 M Na-Cacodylate for 10 minutes. Afterward, the cells were dehydrated using an ascending ethanol series ending in 100% ethanol (15 minutes in each of five ethanol solutions), and

then in propylene oxide for 15 minutes. After dehydration, the cells were infiltrated with a 50:50 solution of propylene oxide: Poly/Bed 812 for 6-24 hr. Then, the cells were embedded in 100% Poly/Bed 812, and placed in 60 ºC oven for at least 48 hr to cure. Finally, the samples were cut to 90-150 nm thick sections for TEM imaging. The images were acquired using a JEOL JEM 1400 TEM (JEOL Ltd., Tokyo, Japan).

4.3 Drugs: Sphingosine Kinase Inhibitors

Human cancer tissues elevate sphingosine kinase (isoforms: SphK1 and SphK2), which results in increased production of sphingosine-1-phosphate (S1P) from sphingosine. These sphingolipid metabolites are involved in diverse cellular processes [113] as well as cancer pathogenesis and treatment [114]. We have previously determined their differential effects on the biomechanical properties of cells as they transition to cancer [76]. S1P is a ubiquitous signaling molecule that acts as a ligand for five G-protein coupled receptors (S1P1-5) whose downstream effects are implicated in a variety of important pathologies including cancer, inflammation, and fibrosis. S1P is an important molecule that controls vascular barrier function, vascular tone, and regulation of lymphocyte trafficking by acting through S1P receptors. The ability of S1P (hence, SphK) to alter the permeability of vascular system is important in cancer metastasis. The synthesis of S1P is catalyzed by SphK and hence, inhibitors of this phosphorylation step are pivotal in not only understanding but also in halting the metastatic transition of cancer cells.

The most potent and selective SphKIs including SphKI1 and SphKI2 as well as a dual inhibitor (DuaLI) were discovered and synthesized by Santos's group [115-117]. SphKIs (chemical formula in Figure 4.1.A) were dissolved in Dimethyl sulfoxide (DMSO) solvent before use as a concentrated stock solution at 4 ºC which was diluted into cell culture medium for conventional free-drug delivery. Alternatively, the SphKIs were incorporated into NPs as detailed below.

4.4 Nanoparticles Fabrication and Characterization

Drug-loaded biodegradable PLGA NPs were fabricated by fluidic nanoprecipitation method [20]. In brief, 1 mL DMSO/acetone (1:9 v/v) dissolving 25 mg PLGA and 5 mg of each SphKI were injected into 5 mL 0.5% Polyvinyl Alcohol (PVA)

solution perpendicularly under continuous stirring (1200 rpm). The resulted suspension was stirred overnight to allow complete acetone evaporation. NPs with about 150 nm mean diameter were collected by centrifugation for 30 min at 10,000 *g*, and were washed for three times using ultrapure water. NPs without drugs were prepared using the same method. Drug loading efficiency was determined by disrupting NPs using 1 M NaOH followed by HPLC analysis. Drug release was detected by dialyzing 8 mg drug loaded NPs against 50 mL 10 mM PBS buffer (pH 7.4) using a dialysis tube with MWCO of 6000-8000 daltons, and the profiles were shown in Figure 4.1.B. Subsequently, the transmission electron microscopy (TEM) image of the PLGA NPs and the distribution of their accommodation in one cell were monitored as shown in Figure 4.1.C.

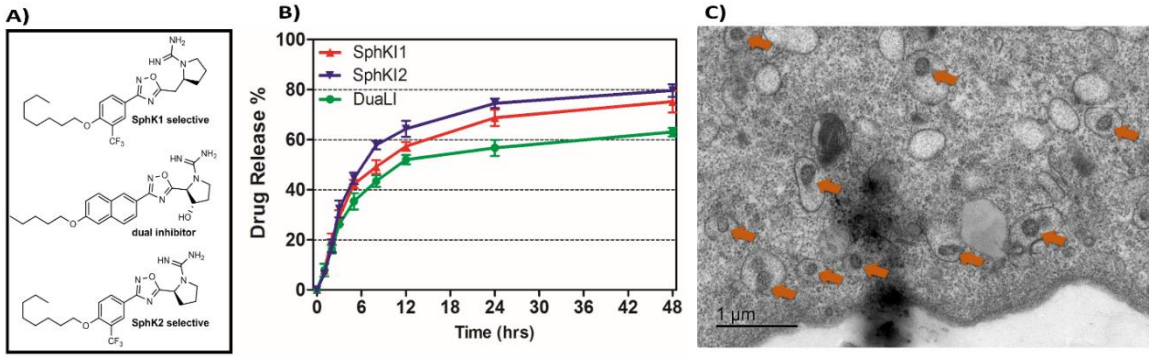

Figure 4.1 A) Formula of the drugs loaded in NPs. B) Release profiles of drug-loaded NPs. C) TEM image of NPs uptake in one cell.

4.5 Data Statistical Analysis

After data acquisition, a MATLAB program (see Appendix) was used to calculate cell entry and travel time through the microchannel, and impedance change magnitude at each frequency for single cells. The curve fitting for extracting cell electrical parameter values were performed using a MATLAB program (see Appendix) based on the nonlinear least squares method ($R^2 > 0.95$). The experiments were conducted for populations with >100 cells from each sample at three separate microfluidic tests. *P*-values between the different populations were calculated using two independent samples t-tests ($\alpha = 0.05$). Results in graphs are presented as arithmetic mean ± standard error of the mean (SEM). All statistical tests were performed using GraphPad Prism software (Graphpad Software Inc., La Jolla, CA).

5 Results and Discussions

5.1 Cell Bioelectrical Characterization

5.1.1 Cell Bioimpedance

The impedance data were measured simultaneously at the four frequencies as single cells move through the constriction channel. Figure 5.1(A-H) shows the mean ± SEM of the maximum changes in the impedance magnitude occurring at different time lapses after treatments at each frequency. There was a significant increase in the mean impedance magnitude of the MDA-MB-231 cells after conventional delivery of either of the three SphKIs. The increase was more pronounced at higher frequencies. In comparison, no significant differences in the mean values of the impedance magnitude occurred in the cells treated with unloaded NPs. Thus, the presence of NPs inside the cells did not measurably change their bioelectrical characteristics. The mean impedance magnitudes of the MDA-MB-231 cells after exposure to NP-packaged SphKIs were similar to those seen for the conventional (free-drug) delivery at all frequencies. It was previously observed that that the impedance magnitude of the tumorigenic cells was on average significantly lower than that of non-tumorigenic cells [101]; the results here, show that the SphKIs raise the impedance magnitude of the highly aggressive breast MDA-MB-231 cells to values more typical of a less tumorigenic phenotype.

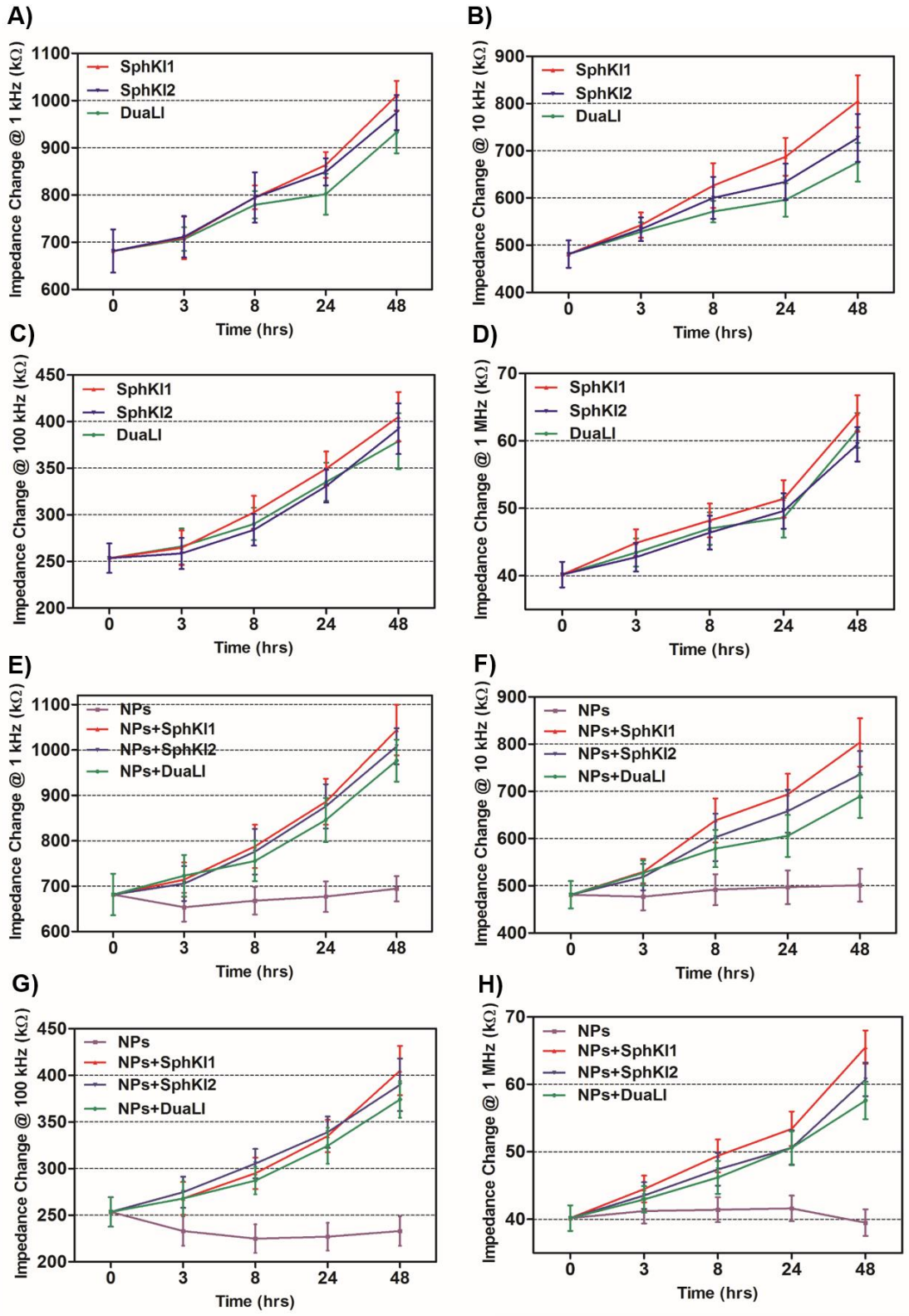

Figure 5.1 Measured impedance changes at 1 kHz, 10 kHz, 100 kHz, and 1 MHz frequency recorded as single MDA-MB-231 cells after NP-packaged and conventional drug-free treatments pass through the constriction channel.

5.1.2 Cell Bioelectrical Parameters

The electric circuit model for the constriction microchannel with an elongated cell shown in Figure 5.2 is used to extract cell bioelectrical parameters [118]. The baseline impedance occurs when no cells are present near the electrodes and the peak impedance occurs when a cell is located in the middle of constriction channel. The electric circuit used to model the microchannel consists of the capacitance of the double layers formed at the interface of the electrodes (C_{dl1}, C_{dl2}) in series with the spreading resistance (R_{sp}) of the culture medium in the constriction channel. A parallel parasitic capacitance (C_{par}) is also considered in the microchannel circuit model. For the living cell, the cell membrane can be modeled as a capacitance (C_m) and the cell cytoplasm as a resistance (R_{cyt}) [118]. A resistance is also present in the path of current flow in the interface of the cell and the wall of the constriction channel which is represented by the interface resistance (R_{int}). As a note, all capacitors in this electrochemical circuit are generally modeled as constant phase elements. C_{dl}, C_{par} and R_{sp} were obtained initially using the baseline impedance. They were later used to obtain C_m, R_{cyt} and R_{int} using the peak impedance. The specific membrane capacitance was obtained by dividing the membrane capacitance by surface area of cell head and tail in the constriction channel which are estimated as the hemispherical surface area ($4\pi r^2$ where r=4 μm). The cytoplasm conductivity was obtained from $l/(R_{cyt}.A)$ where l is the cell length in the channel and A is the channel cross section area ($8\times8\ \mu m^2$).

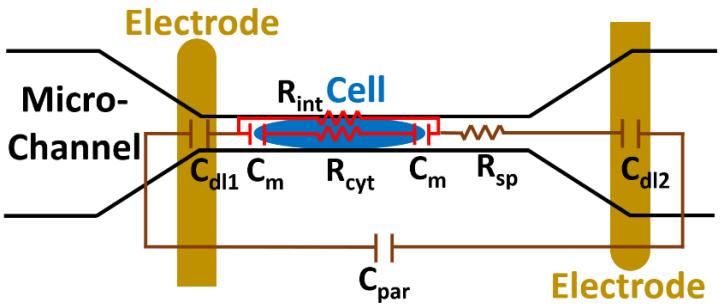

Figure 5.2 A Schematic illustration of the electric circuit model for the microchannel with an elongated cell used to characterize cell electrical parameters from the multi-frequency impedance measurements. Circuit element legend: C_{dl1} and C_{dl2}- double layer capacitance; C_{par}- parasitic capacitance; C_m- membrane capacitance; R_{sp}- spreading resistance; R_{cyt}- cytoplasm resistance; R_{int}- cell-channel wall interface resistance.

The model presented in Figure 5.2 was fitted to the data from the multi-frequency impedance measurements to extract the cell bioelectrical parameters. The interface resistance, specific membrane capacitance, and cytoplasm conductivity of the MDA-MB-231 cells after a 48-hr treatment with free-drug and NP-packaged SphKIs in comparison to untreated and unloaded NP-treated cells, respectively, are extracted and depicted in Figure 5.3(A-C). According to Figure 5.3.A, interface resistance (R_{int}) is significantly larger after both conventional free-drug and NP-packaged delivery of SphKI1, SphKI2, and DuaLI. Thus, treatment of the breast cancer cells with SphKIs increased the resistance at the interface between the cell and the channel wall, which might reflect increased surface friction. Our previous results also showed that non-tumorigenic cells have significantly higher R_{int} values compared to the highly metastatic cells (unpublished data). In addition, as shown in Figure 5.3.B, the cells treated with one of SphKIs, regardless of delivery method exhibited on average a significantly lower specific membrane capacitance. The membrane capacitance can be changed due to alterations in lipid composition, surface charges, and ion channel regulation [119]. The membrane of tumorigenic cell is found relatively enriched in many kinds of lipids [120], which causes tumorigenic cells to show an increased membrane capacitance [121, 122]. In fact, as a result of SphKIs treatment, the bioactive sphingolipid metabolite, S1P is expected to be diminished. Previously published results showed that S1P increases cell membrane capacitance.[123]. Since SphK catalyses formation of S1P, hence inhibition of SphK might explain reversal of the membrane capacitance of the breast cancer cells following treatments with the three SphKIs. The cytoplasm conductivity is another extracted parameter reflecting the cell interior's bioelectrical properties. Notably, the cytoplasmic conductivity of the breast cancer cells did not considerably change after SphKIs treatment. This suggests that either the possible reorganization of internal cytoskeleton by SphKIs or the presence of NPs in cell's cytoplasm did not cause significant changes in the cell's bioelectrical conductivity. Taken together, the reported trend of changes in the bioelectrical parameters of the MDA-MB-231 cells after treatment with SphKIs indicate a shift

in the interface resistance and the membrane capacitance of the highly aggressive MDA-MB-231 cells toward their less tumorigenic phenotype.

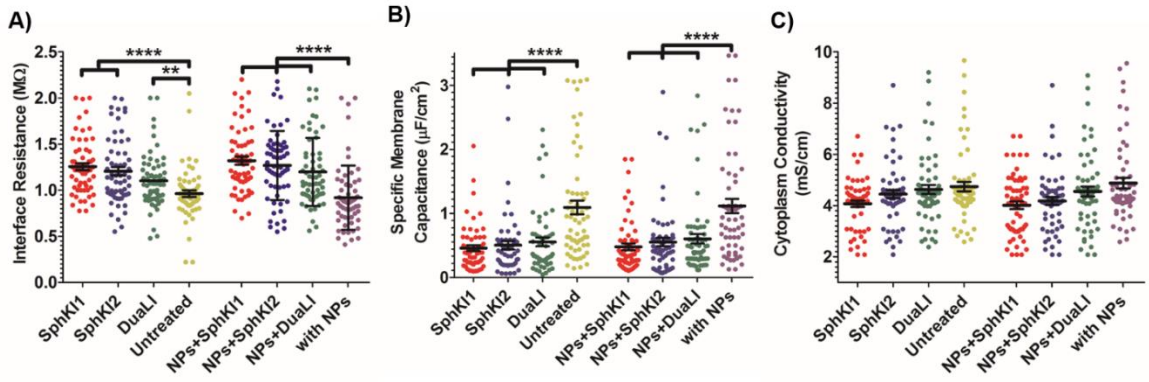

Figure 5.3 Scatter plots of (A) Interface resistance, (B) specific membrane capacitance, and (C) cytoplasm conductivity obtained for 48-hr treated cells with free-drug and NP-packaged SphKIs in comparison to untreated and unloaded NPs-treated cells, respectively. **$P<0.01$, ****$P<0.0001$.

5.2 Cell Biomechanical Characterization

5.2.1 Cell Deformability Indices

Total transit time of the cells through the constriction channel can be broken down to entry and travel times. The entry and travel time stamps can provide information about cell deformability and viscoelasticity, hence the cell biomechanical properties [124, 125], as the cells must completely deform and squeeze into the constriction channel. Figure 5.4.A shows the entry times of cells at different time lapses after conventional free-drug and NP-packaged delivery. The travel times through the constriction channel are also shown in Figure 5.4.B which followed a pattern similar to the entry time for different samples. Impedance data was used to track entry and travel times. The entry times for the MDA-MB-231 cell population continuously deceased by time after free-drug treatments with the three SphKIs. These measurements indicate that the mean ± SEM of entry times for the highly metastatic MDA-MB-468 cells (2.072±0.217 s) became statistically shorter ($P<0.01$) after 48-hr free-drug treatments with SphKI1 (1.285±0.165 s), SphKI2 (1.493±0.233 s), and DuaLI (1.389±0.172 s). The travel times of the MDA-MB-231 cells through the microchannel was 0.711±0.087 s which decreased to 0.441±0.080 s, 0.490±0.072 s, 0.472±0.071 s ($P<0.05$) after free-drug treatments with SphKI1, SphKI2, DuaLI, respectively. Some previously published AFM-

based stiffness measurements also reported that S1P can increase the stiffness of cells to some extent [126, 127]. Since SphK catalyses the formation of S1P, inhibitors of SphK can have opposite effects on the cell stiffness which justifies the decrease in cell deformability as a result of treatment with the three SphKIs. In contrast, after NP-packaged treatments of the MDA-MB-231 cells, there was an initial increase in the entry times followed by decrease in the convening hours when the SphKIs are released. The initial rise in the entry time is because of the absorbance of NPs while the following decreases are apparently because the effects of the released drugs dominated the effects of internalized NPs. According to the results, the cells showed longer entry time after 3-hr treatment with unloaded NPs, although this increasing trend was lower after the initial 3 hr probably because the NPs' internalization rate decreases. This 3-hr time is enough for the NPs to be up taken by the cells. The increase in the stiffness of different cells under the impact of NPs was previously shown [15-17].

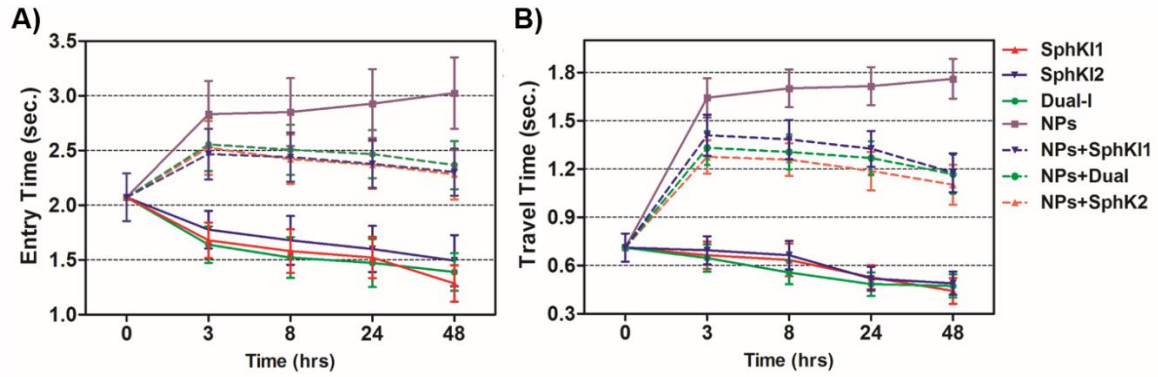

Figure 5.4 Measured A) entry time and B) travel time changes recorded as single MDA-MB-231 cells before and after treatments pass through the constriction channel.

5.2.2 Cell Cytoskeleton Evaluation

Cell biomechanical changes are attributed to the reorganization of the cell cytoskeletal proteins where actin filaments have been found to play the dominant role [75]. Actin filament structure organizations were monitored using immunofluorescent staining to correlate the changes in the cell deformability to the alterations in their intracellular cytoskeleton. Figure 5.5(A-E) shows the actin filaments of the untreated cells compared to the cells after SphKIs and NPs treatments.

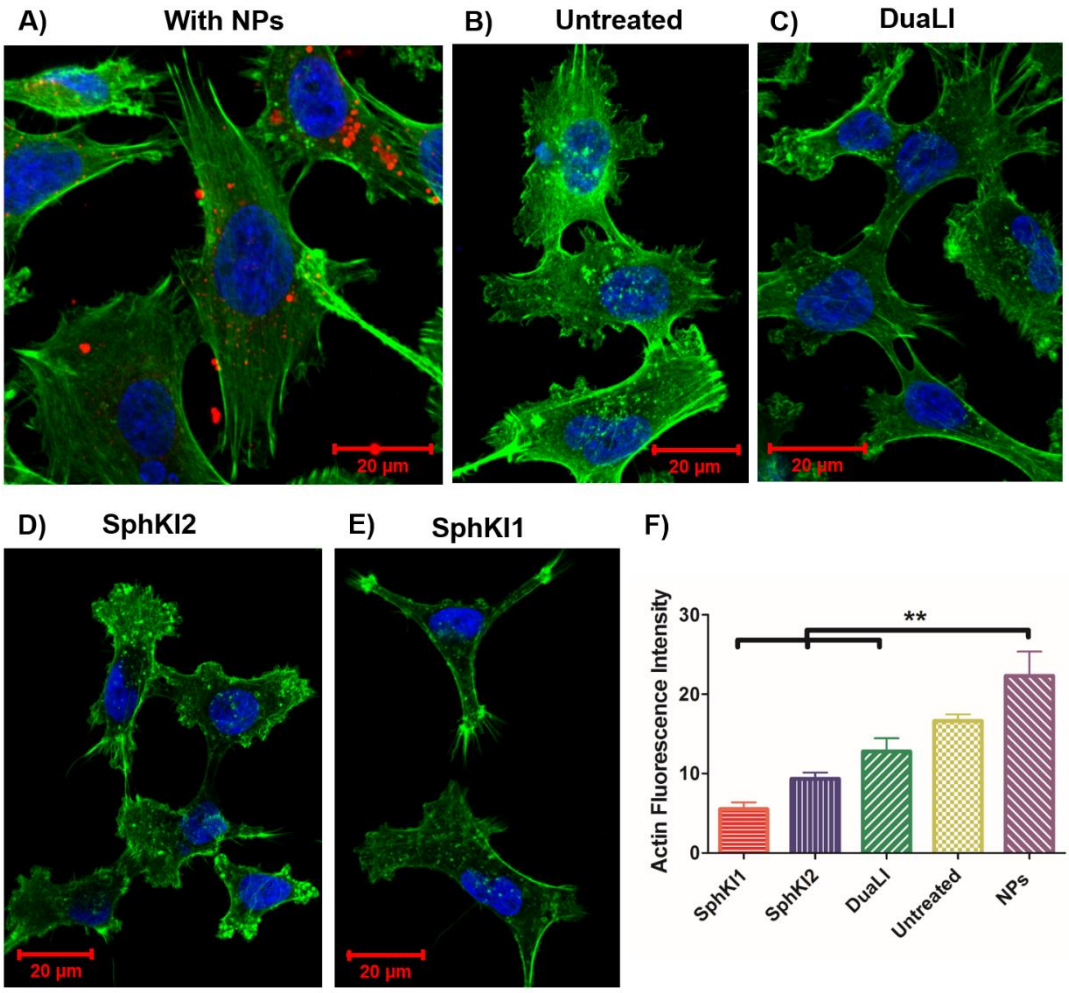

Figure 5.5 Immunofluorescence images showing difference in the actin organization of A) unloaded NP-treated, B) untreated, C) DuaLI treated, D) SphKI2 treated, and E) SphKI1 treated cells. F) Actin content intensity revealed treatments with SphKI, SphKI2, and DuaLI led to a decrease in the actin intensity, while the absorbed NPs increased the actin intensity.

Accordingly, while the presence of NPs considerably regulated actin fiber organization, SphKIs treatment deregulated them. Moreover, the actin filament relative intensity from fluorescence staining was measured to identify the contribution of these changes in biomechanical properties of cells, and the results are shown in Figure 5.5.F. The intensity decreased after SphKIs treatment. This value was 16.6 for the untreated aggressive MDA-MB-231 cells while reduced to 5.5, 9.3, and 12.7 after treatments with SphKI1, SphKI2, and DuaLI, respectively. Furthermore, the level of fluorescence intensity for the cells noticeably increased to 22.3 after unloaded NPs treatment. In other words, treatment with the SphKIs

reduces the actin microfilament intensity by approximately 66%, 44%, and 23%, for SphKI1, SphKI2, and DuaLI, respectively, while the presence of NPs led to an increase in the content of actin by 34%.

WB analysis was also performed to quantify the relative actin content of cells. Figure 5.6.A shows the results of WB analysis. Figure 5.6.B shows the relative band intensities of the samples normalized to the largest one. Accordingly, treatments with SphKI1, SphKI2, and DuaLI led to a decrease in the actin content by approximately 33%, 17% and 14%, respectively. In contrast, the level of actin was 11% higher in the cells treated with unloaded NPs than that of the untreated cells. It can be concluded that treatments with SphKIs decrease the level of actin filaments, while NPs increase this level.

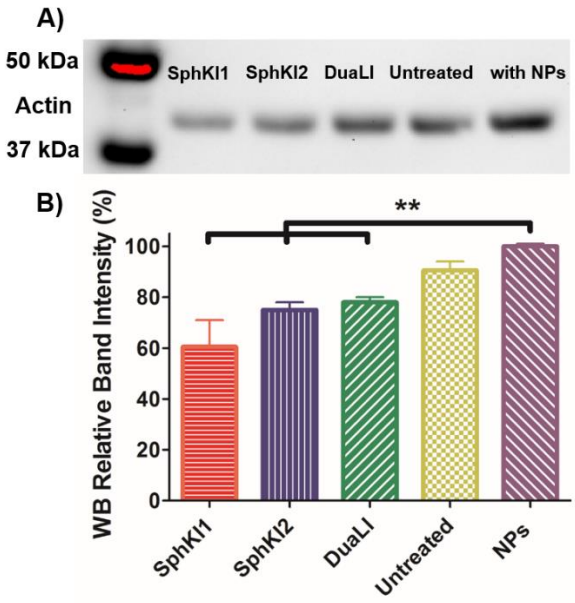

Figure 5.6 A) actin filaments protein WB of whole-cell extracts from untreated cells and cells treated with SphKI1, SphKI2, DuaLI, and unloaded NPs for 48 hr. B) Normalized (to with unloaded-NPs) levels of actin protein bands in treated and untreated cells.

6 Conclusions and Future Work

A microfluidic chip was in this thesis developed for high-throughput label-free measurements of biomechanical and bioelectrical properties of single cells. The microchip includes an electrode pair embedded on either sides of a narrow constriction channel which serves the dual purpose of automating the entry and travel time measurements and enabling multi-frequency impedance measurements simultaneously as single cells pass continuously through the constriction channel. The microchip was used in this study for characterization of single-cell biophysical properties of human breast cancer cells in response to SphKIs and quantify the effectiveness of NP-packaged SphKI in cell populations. The effects of three newly developed SphKIs following conventional free-drug delivery and NP-packaged drugs in a highly metastatic cell line, MDA-MB-231, were compared using this microchip. Significant increases were observed in the impedance magnitude of SphKI-treated cells at all frequencies, regardless of the drug delivery approach. The bioelectrical parameters extracted by fitting the impedance measurements of individual cells made at four frequencies to an electrical circuit model indicated that SphKI, but not NPs, produced significant differences in cell-channel interface resistance and specific membrane capacitance of the cells. With respect to the biomechanical properties, the entry and travel times of the cells slightly decreased in cells after SphKIs free-drug treatments, but increased following SphKIs NP-packaged treatments. We observed that the NPs alone modulated the cell biomechanical characteristics, and such biomechanical alterations might involve reorganization and changes in the content of the cell cytoskeletal actin as determined by immunofluorescence and WB analysis. The approach of this work can be used to screen therapeutic avenues for the ability to reverse the biophysical traits that take place during cancer progression. The work here shows how the combination of single-cell biophysical (bioelectrical and biomechanical) analyses with drug screening might provide a promising strategy to identify new genres of cancer therapeutics that possess capabilities to reverse biophysical changes that take place during cancer progression.

The suggestions and ideas for the future works can be classified into three parts of device performance improvement, modeling development, and device application extension.

Regarding to the device performance improvement, a lot of works can be done in the future in order to improve sensitivity, resolution, throughput, and content of the microchip. In order to achieve a high-throughput device, a platform with parallel constriction test channels is suggested for the analysis of a larger number of cells.

The current sampling rate of the integrated electrode pair is limited to 250 Hz (or 4 milli-sec) which confines their resolution in data acquisition. On the other hand, relying on high-speed camera imaging, not only deprives us of the cell bioelectrical information, the recording video time is typically very short at high resolutions (e.g. only 2.5 sec for 1000 fames/sec sampling rate) which limits the number of imaged cells in one video. Taken together, improving sampling rate of the electrode pair can keep the automation of the microchip and in addition enhance the differentiation capability of the microchip.

The geometry or shape of the constriction channel can also be changed from a straight channel to other non-straight shapes such as a wavy or a multi-segments channel. Under the varying environmental mechanical forces that the cells experience while passing through a non-straight channel, the cells continually modify their cytoskeleton architecture in such a way that allows them to adapt their biomechanical properties to compensate for environmental forces. Distinct biomechanical responses of normal and cancer cells in face of these time-varying forces may provide more powerful biomarkers for differentiation of single cancer cell using the microchip.

The configuration of the embedded electrodes can also be altered in order to achieve a higher sensitivity in bioimpedance measurements of the individual cell. It may also lead to gain more information about the cells including their detailed speed or location in the constriction channel or even their relative size. All these content-rich biophysical information can provide more strength biomarker for distinction between the individual cells. Another issue concerns the fact that the cell size is an effective factor in entry/travel times measured in this designed microfluidic device. New configuration of the electrode pair or an additional electrode near the entry of the test channel may facilitate cell size measurement. Size-based sorting of cell population before feeding the

microchip or in the microchip using a mechanism can also alleviate this issue and make the comparisons of the measured biophysical markers between the tested cells to be more rational. The mechanisms which can be proposed is a staggered set of posts near the entrance of test channel, which will restrict the entry of large or aggregated cells. Another option is utilizing hydrodynamic effects in a curved microchannel for size-based cell separation.

All these improvements in the device performance along with implementation of a portable integrated circuit for impedance measurements and a fluidic control system can provide the opportunity of building a portable single-cell-analysis assay for clinical application.

One challenge for microfluidic-based measurements presently lies in the weak correlation between cell biophysical properties and the widely used biophysical markers. Precise modeling on the microfluidic-based measurements must be well established before the measurements can be understood and interpreted and practically be accepted as a clinical marker. We have presented an electric circuit model in this thesis for the microchannel and cell used to characterize cell bioelectrical parameters from impedance measurements which can be improved by considering more details in the modeling or employing a finite element method. On the other hand, although the entry/travel times of a cell is considered as a qualitative indicator of cell deformability, it is still unclear how this entry/travel times are related analytically to the mechanical properties of the cell. Resolving this issue requires a mathematical model (either analytical models or numerical simulation) describing the relationship between the entry/travel times and the elasticity and viscosity of a cell in the context of the channel geometry.

Finally, the application of biosensor microchip developed in this thesis as a diagnostic assay can be extended to explore other cancer cell types, cancer stem/tumor initiating cells, and primary human cancer cells or even beyond cancer application to many other diseases such as malaria, sepsis, diabetes, etc. that directly impact and deregulate cell biophysics as a consequence of changes induced in cell membrane, cytoskeleton, and cytosol. Moreover, the microchip can be employed for other screening and monitoring applications including monitoring of environmental toxicants and/or efficacy screening of many biologically active chemical agents and pharmaceutics.

References

[1] H. Babahosseini, A. K. Ketene, E. M. Schmelz, P. C. Roberts, M. Agah. Biomechanical profile of cancer stem-like/tumor-initiating cells derived from a progressive ovarian cancer model. Nanomedicine: NBM. 2014;10:1013-9.
[2] B. Carmichael, H. Babahosseini, S. N. Mahmoodi, M. Agah. The fractional viscoelastic response of human breast tissue cells. Phys Biol. 2015;12:046001.
[3] H. Babahosseini, B. Carmichael, J. S. Strobl, S. N. Mahmoodi, M. Agah. Sub-cellular force microscopy in single normal and cancer cells. Biochem Biophys Res Commun. 2015;463:587–92.
[4] A. N. Ketene, E. M. Schmelz, P. C. Roberts, M. Agah. The effects of cancer progression on the viscoelasticity of ovarian cell cytoskeleton structures. Nanomedicine: NBM. 2012;8:93-102.
[5] K. Heileman, J. Daoud, M. Tabrizian. Dielectric spectroscopy as a viable biosensing tool for cell and tissue characterization and analysis. Biosens Bioelectron. 2013;49:348–59.
[6] Y. Zhao, D. Chen, Y. Luo, H. Li, B. Deng, S. B. Huang, et al. A microfluidic system for cell type classification based on cellular size-independent electrical properties. Lab Chip. 2013;13:2272-7.
[7] J. Wanga, Z. Wan, W. Liu, L. Li, L. Ren, X. Wang, et al. Atomic force microscope study of tumor cell membranes following treatment with anti-cancer drugs. Biosens Bioelectron. 2009;25:721-7.
[8] L. Xiao, M. Tang, Q. Li, A. Zhou. Non-invasive detection of biomechanical and biochemical responses of human lung cells to short time chemotherapy exposure using AFM and confocal Raman spectroscopy. Anal Methods. 2012;5:874-9.
[9] S. Sharma, C. Santiskulvong, L. A. Bentolila, J. Rao, O. Dorigo, J. K. Gimzewski. Correlative nanomechanical profiling with super-resolution F-actin imaging reveals novel insights into mechanisms of cisplatin resistance in ovarian cancer cells. Nanomedicine. 2012;8:757-66.
[10] S. E. Cross, Y. S. Jin, Q. Y. Lu, J. Rao, J. K. Gimzewski. Green tea extract selectively targets nanomechanics of live metastatic cancer cells. Nanotechnology. 2011;22:215101.
[11] T. Watanabe, H. Kuramochi, A. Takahashi, K. Imai, N. Katsuta, T. Nakayama, et al. Higher cell stiffness indicating lower metastatic potential in B16 melanoma cell variants and in (–)-epigallocatechin gallate-treated cells. J Cancer Res Clin Oncol. 2012;138:859-66.
[12] W. H. De Jong, P. J. A. Borm. Drug delivery and nanoparticles: Applications and hazards. Int J Nanomedicine. 2008;3:133-49.
[13] T. Sun, Y. S. Zhang, B. Pang, D. C. Hyun, M. Yang, Y. Xia. Engineered Nanoparticles for Drug Delivery in Cancer Therapy. Angewandte Chemie International Edition. 2014;53:12320-64.
[14] K. Cho, X. Wang, S. Nie, Z. (G.) Chen, D. M. Shin. Therapeutic Nanoparticles for Drug Delivery in Cancer. Clin Cancer Res. 2008;14:1310-6.
[15] I. V. Ogneva, S. V. Buravkov, A. N. Shubenkov, L. B. Buravkova. Mechanical characteristics of mesenchymal stem cells under impact of silica-based nanoparticles. Nanoscale Res Lett. 2014;9:283.

[16] W. Zhang, J. Hughes, Y. Chen. Impacts of Hematite Nanoparticle Exposure on Biomechanical, Adhesive, and Surface Electrical Properties of Escherichia coli Cells. Appl Environ Microbiol. 2012;78:3905-15.
[17] K. Buyukhatipoglu, A. M. Clyne. Superparamagnetic iron oxide nanoparticles change endothelial cell morphology and mechanics via reactive oxygen species formation. J Biomed Mater Res A. 2011;96:186-95.
[18] J. Pi, F. Yang, H. Jin, X. Huang, R. Liu, P. Yang, et al. Selenium nanoparticles induced membrane bio-mechanical property changes in MCF-7 cells by disturbing membrane molecules and F-actin. Bioorg Med Chem Lett. 2013;23:6296-303.
[19] S. Pyne, R. Bittman, N. J. Pyne. Sphingosine Kinase Inhibitors and Cancer: Seeking the Golden Sword of Hercules. Cancer Res. 2011;71:6576-82.
[20] W. Huang, J. Zhang, H. C. Dorn, C. Zhang. Assembly of bio-nanoparticles for double controlled drug release. PLoS One. 2013;8:e74679.
[21] Y. Hu, M. Ehrich, K. Fuhrman, C. Zhang. In vitro performance of lipid-PLGA hybrid nanoparticles as an antigen delivery system: lipid composition matters. Nanoscale Res Lett. 2014;9:434.
[22] Y. Matsumura, H. Maeda. A new concept for macromolecular therapeutics in cancer chemotherapy: mechanism of tumoritropic accumulation of proteins and the antitumor agent smancs. Cancer Res. 1986;46:6387-92.
[23] A. J. Cole, V. C. Yang, A. E. David. Cancer theranostics: the rise of targeted magnetic nanoparticles. Trends Biotechnol. 2011;29:323-32.
[24] J. W. Yoo, C. Elizabeth, M. Samir, Des. 2012, . Factors that Control the Circulation Time of Nanoparticles in Blood: Challenges, Solutions and Future Prospects. Curr Pharm. 2012;16:2298-307.
[25] A. Kumari, S. K. Yadav, S. C. Yadav. Biodegradable polymeric nanoparticles based drug delivery systems. Colloids Surf B Biointerfaces. 2010;75:1-18.
[26] Panyam J, Labhasetwar V. Biodegradable nanoparticles for drug and gene delivery to cells and tissue. Adv Drug Deliv Rev. 2003;55:329-47.
[27] des Rieux A, Fievez V, Garinot M, Schneider YJ, V P. Nanoparticles as potential oral delivery systems of proteins and vaccines: a mechanistic approach. J Control Release. 2006;116:1-27.
[28] T. Sun, Y. S. Zhang, B. Pang, D. C. Hyun, M. Yang, Y. Xia. Engineered Nanoparticles for Drug Delivery in CancerTherapy. Angew Chem Int Ed. 2014;53:12320-64.
[29] F. Y. Cheng, C. H. Su, P. C. Wu, C. S. Yeh. Multifunctional polymeric nanoparticles for combined chemotherapeutic and near-infrared photothermal cancer therapy in vitro and in vivo. Chem Commun (Camb). 2010;46:3167–9.
[30] H. Yang, K. Li, Y. Liu, Z. Liu, H. Miyoshi. Poly(D,L-lactide-co-glycolide) nanoparticles encapsulated fluorescent isothiocyanate and paclitaxol: preparation, release kinetics and anticancer effect. J Nanosci Nanotechnol. 2009;9:282-7.
[31] J. M. Koziara, P. R. Lockman, D. D. Allen, R. J. Mumper. Paclitaxel nanoparticles for the potential treatment of brain tumors. J Control Release. 2004;99:259–69.
[32] L. Barraud, P. Merle, E. Soma, L. Lefrancois, S. Guerret, M. Chevallier, et al. Increase of doxorubicin sensitivity by doxorubicin-loading into nanoparticles for hepatocellular carcinoma cells in vitro and in vivo. J Hepatol. 2005;42:736–43.

[33] D. A. Fletcher, R. D. Mullins. Cell mechanics and the cytoskeleton. Nature. 2010;463:485-92.
[34] H. D. Huang, R. D. Kamm, R. T. Lee. Cell mechanics and mechanotransduction: pathways, probes, and physiology. Am J Physiol Cell Physiol. 2004;287:C1-C11.
[35] P. A. Janmey, C. A. McCulloch. Cell mechanics: integrating cell responses to mechanical stimuli. Annu Rev Biomed Eng 2007;9:1-34.
[36] R. McBeath, D. M. Pirone, C. M. Nelson, K. Bhadriraju, C. S. Chen. Cell shape, cytoskeletal tension, and RhoA regulate stem cell lineage commitment. Dev Cell. 2004;6:483-95.
[37] K. Kaibuchi, S. Kuroda, M. Amano. Regulation of the cytoskeleton and cell adhesion by the Rho family GTPases in mammalian cells. Annu Rev Biochem 1999;68:459-86.
[38] M. Nikkhah, J. Strobl, B. Peddi, M. Agah. Cytoskeletal Role in Differential Adhesion Patterns of Normal Fibroblasts and Breast Cancer Cells inside Silicon Microenvironments. Biomed Microdevices. 2009;11:585-95.
[39] A. J. Ridley, M. A. Schwartz, K. Burridge, R. A. F, M. H. G, G. B, et al. Cell migration: integrating signals from front to back. Science. 2003;302:1704-9.
[40] D. Yamazaki, S. Kurisu, T. Takenawa. Regulation of cancer cell motility through actin reorganization. Cancer Sci. 2005;96:379-86.
[41] M. A. Wozniak, C. S. Chen. Mechanotransduction in development: a growing role for contractility. Nat Rev Mol Cell Biol 2009;10:34-43.
[42] R. A. Desai, L. Gao, S. Raghavan, W. F. Liu, C. S. Chen. Cell polarity triggered by cell-cell adhesion via Ecadherin. J Cell Sci. 2009;122:905-11.
[43] D. E. Ingber. Mechanobiology and diseases of mechanotransduction. Ann Med. 2003;35:564-77.
[44] P. C. Roberts, E. Motillo, A. C. Baxa, H. H. Q. Heng, N. Doyon-Reale, L. Gregoire, et al. Sequential Molecular and Cellular Events during Neoplastic progression: A Mouse Syngeneic Ovarian Cancer Model. Neoplasia. 2005;7:944-56.
[45] K. A. Ward, W. I. Li, S. Zimmer, T. Davis. Viscoelastic properties of transformed cells: role in tumor cell progression and metastasis formation. Biorheology. 1991;28:301-13.
[46] S. Suresh. Biomechanics and biophysics of cancer cells. Acta Biomater. 2007;3:413-38.
[47] J. B. Wyckoff, J. G. Jones, J. S. Condeelis, J. E. Segall. A critical step in metastasis: in vivo analysis of intravasation at the primary tumor. Cancer Res. 2000;60:2504-11.
[48] A. A. Shah-Yukich, A. C. Nelson. Characterization of solid tumor microvasculature: a three-dimensional analysis using the polymer casting technique. Lab Invest. 1988;58:236-44.
[49] A. L. Creekmore, W. T. Silkworth, D. Cimini, R. V. Jensen, P. C. Roberts, E. M. Schmelz. Changes in gene expression and cellular architecture in an ovarian cancer progression model. PLoS ONE. 2011;6:e17676.
[50] B. D. Hoffman, J. C. Crocker. Cell mechanics: dissecting the physical responses of cells to force. Annu Rev Biomed Eng. 2009;11:259-88.
[51] C. T. Lim, E. H. Zhou, S. T. Quek. Mechanical models for living cells-a review. J Biomech. 2006;39:195-216.

[52] A. E. Pelling, M. A. Horton. An historical perspective on cell mechanics. Pflugers Arch. 2008;456:3-12.
[53] C. T. Lim, E. H. Zhou, A. Li, S. R. K. Vedula, H. X. Fu. Experimental techniques for single cell and single molecule biomechanics. Mater Sci Eng C, Biomim Supramol Syst. 2006;26:1278-88.
[54] M. A. Teitell, K. Sheraz, J. Schmit, J. Reed. Biomechanics of single cells and cell populations. In: Ho. D, editor. Nanodiamonds: Applications in biology and Nanoscale Medicine2010. p. 235-46.
[55] M. Lekka, P. Laidler, D. Gil, J. Lekki, Z. Stachura, A. Z. Hrynkiewicsm. Elasticity of normal and cancerous human bladder cells studied by scanning force microscopy. Biophys J. 1999;28:312-6.
[56] S. Sen, S. Subramanian, D. E. Discher. Indentation and adhesive probing of a cell membrane with AFM: theoretical model and experiments. Biophys J. 2005;89:3203-13.
[57] E. M. Darling, S. Zauscher, J. A. Block, F. Guilak. A Thin-Layer Model for Viscoelastic, Stress-Relaxation Testing of Cells Using Atomic Force Microscopy: Do Cell Properties Reflect Metastatic Potential? Biophys J. 2007;92:1784-91.
[58] M. Radmacher, M. Frtiz, C. M. Kacher, J. P. Cleveland, H. G. Hansma. Measuring the viscoelastic properties of human platelets with the atomic force microscope. Biophys J. 1996;70:556-67.
[59] R. M. Hochmuth. Micropipette aspiration of living cells. J Biomech. 2000;33:15-22.
[60] O. Thoumine, A. Ott. Time scale dependent viscoelastic and contractile regimes in fibroblasts probed by microplate manipulation. J Cell Sci. 1997;110:2109-16.
[61] N. Wang, D. E. Ingber. Probing transmembrane mechanical coupling and cytomechanics using magnetic twisting cytometry. Biochem Cell Biol. 1995;73:327-35.
[62] D. R. Overby, B. D. Matthews, E. Alsberg, D. E. Ingber. Novel Dynamic rheological behavior of individual focal adhesions measured within single cells using electromagnetic pulling cytometry. Acta Biomater. 2005;1:295-303.
[63] M. Dao, C. T. Lim, S. Suresh. Mechanics of the human red blood cell deformed by optical tweezers. J Mech Phy Solids. 2003;51:2259-80.
[64] J. Guck, S. Schinkinger, B. Lincoln, F. Wottawah, S. Ebert, M. Romeyke, et al. Optical deformability as an inherent cell marker for testing malignant transformation and metastatic competence. Biophys J. 2005;88:3689-98.
[65] D. J. Muller, Y. F. Dufrene. Atomic force microscopy as a multifunctional molecular toolbox in nanobiotechnology. Nat Nanotechnol. 2008;3:261-9.
[66] K. D. Costa. Single-cell elastography: probing for disease with the atomic force microscope. Dis Markers. 2003;19:139-54.
[67] Suresh S. Biomechanics and biophysics of cancer cells. Acta Biomaterialia. 2007;3:413-38.
[68] Radmacher M, Frtiz M, Kacher CM, Cleveland JP, Hansma HG. Measuring the viscoelastic properties of human platelets with the atomic force microscope. Biophysics Journal. 1996;70:556-67.
[69] R. E. Mahaffy, S. Park, E. Gerde, J. Kas, C. K. Shih. Quantitative Analysis of the viscoelastic properties of thin regions of fibroblasts using atomic force microscopy. Biophys J. 2004;86:1777-93.

[70] H. Babahosseini, J. S. Strobl, Agah M. Using nanotechnology and microfluidics in search of cell biomechanical cues for cancer progression. Nanomedicine. 2015;10:2635-8.
[71] M. Nikkhah, J. S. Strobl, E. M. Schmelz, R. De Vitad, M. Agah. The cytoskeletal organization of breast carcinoma and fibroblast cells inside three dimensional (3-D) isotropic silicon microstructures. Biomaterials. 2010;31:4552–61.
[72] J. S. Strobla, M. Nikkhahb, Agahb M. Actions of the anti-cancer drug suberoylanilide hydroxamic acid (SAHA) on human breast cancer cytoarchitecture in silicon microstructures. Biomaterials. 2010;31:7043-50.
[73] M. Nikkhaha, J. S. Strobl, E. M. Schmelzc, P. C. Robertsd, H. Zhouc, M. Agah. MCF10A and MDA-MB-231 human breast basal epithelial cell co-culture in silicon micro-arrays. Biomaterials. 2011;32:7625-32.
[74] M. Nikkhah, J. Strobl, E. Schmelz, M. Agah. Evaluation of the influence of growth medium composition on cell elasticity. Biomechanics. 2011;44:762-6.
[75] A. N. Ketene, P. C. Roberts, A. A. Shea, E. M. Schmelz, M. Agah. Actin filaments play a primary role for structural integrity and viscoelastic response in cells. Integr Biol. 2012;4:540-9.
[76] H. Babahosseini, P. C. Roberts, E. M. Schmelz, M. Agah. Bioactive sphingolipid metabolites modulate ovarian cancer cell structural mechanics. Integr Biol. 2013;5:1385-92.
[77] H. Babahosseini, S.S. Strobl, M. Agah. Single cell metastatic phenotyping using pulsed nanomechanical indentations. Nanotechnology. 2015;26:354004.
[78] M. J. Rosenbluth, W. A. Lam, D. A. Fletcher. Analyzing cell mechanics in hematologic diseases with microfluidic biophysical flow cytometry. Lab Chip. 2008;8:1062-70.
[79] Y. Zheng, E. Shojaei-Baghini, A. Azad, C. Wang, Y. Sun. High-throughput biophysical measurement of human red blood cells. Lab Chip. 2012;12:2560-7.
[80] D. R. Gossett, H. T. K. Tse, S. A. Lee, Y. Ying, A. G. Lindgren, O. O. Yang, et al. Hydrodynamic stretching of single cells for large population mechanical phenotyping. Proc Natl Acad Sci USA. 2012;109:7630-5.
[81] N. Bao, G. C. Kodippili, K. M. Giger, V. M. Fowler, P. S. Low, C. Lu. Single-cell electrical lysis of erythrocytes detects deficiencies in the cytoskeletal protein network. Lab Chip. 2011;11:3053-6.
[82] E. Jonietz. Mechanics: The forces of cancer. Nature. 2012;491:S56-S7.
[83] I. Doh, W. C. Lee, Y. H. Cho, A. P. Pisano, F. A. Kuypers. Deformation measurement of individual cells in large populations using a single-cell microchamber array chip. Appl Phys Lett. 2012;100:173702.
[84] Y. Zheng, J. Nguyen, Y. Wei, Y. Sun. Recent advances in microfluidic techniques for single-cell biophysical characterization. Lab Chip. 2013;13:2464-83.
[85] Q. Guo, S. Parka, H. Ma. Microfluidic micropipette aspiration for measuring the deformability of single cells. Lab Chip. 2012;12:2687-95.
[86] A. Adamo, A. Sharei, L. Adamo, B. Lee, S. Mao, K. F. Jensen. Microfluidics-Based Assessment of Cell Deformability. Anal Chem. June 2012;84:6438-43.
[87] J. Chen, Y. Zheng, Q. Tan, E. Shojaei-Baghini, Y. Liang Zhang, J. Li, et al. Classification of cell types using a microfluidic device for mechanical and electrical measurement on single cells. Lab Chip. 2011;11:3174-81.

[88] P. Gascoyne, R. Pethig, J. Satayavivad, F. F. Becker, M. Ruchirawat. Dielectrophoretic detection of changes in erythrocyte membranes following malarial infection. Biochim Biophys Acta - Biomembranes. 1997;1323:240-52.
[89] K. Heileman, J. Daoud, M. Tabrizian. Dielectric spectroscopy as a viable biosensing tool for cell and tissue characterization and analysis. Biosens Bioelectron. 2013;49:348-59.
[90] J. Yang, Y. Huang, X. J. Wang, X. B. Wang, F. F. Becker, P. R. C. Gascoyne. Dielectric properties of human leukocyte subpopulations determined by electrorotation as a cell separation criterion. Biophys J. 1999;76:3307-14.
[91] X. B. Wang, Y. Huang, P. R. C. Gascoyne, F. F. Becker, R. Holzel, R. Pethig. Changes in Friend Murine Erythroleukemia Cell-Membranes during Induced-Differentiation Determined by Electrorotation. Biochim Biophys Acta, Biomembr. 1994;1193:330-44.
[92] D. Zimmermann, A. Zhou, M. Kiesel, K. Feldbauer, U. Terpitz, W. Haase, et al. Effects on capacitance by overexpression of membrane proteins. Biochem Biophys Res Commun. 2008;369:1022-6.
[93] Y. Huang, X. B. Wang, R. Holzel, F. F. Becker, P. R. C. Gascoyne. Electrorotational Studies of the Cytoplasmic Dielectric-Properties of Friend Murine Erythroleukemia-Cells. Phys Med Biol. 1995;40:1789-806.
[94] L. Duncan, H. Shelmerdine, M. P. Hughes, H. M. Coley, Y. Hubner, F. H. Labeed. Dielectrophoretic analysis of changes in cytoplasmic ion levels due to ion channel blocker action reveals underlying differences between drug-sensitive and multidrug-resistant leukaemic cells. Phys Med Biol. 2008;53:N1-N7.
[95] R. Holzel. Non-invasive determination of bacterial single cell properties by electrorotation. Biochim Biophys Acta, Mol Cell Res. 1999;1450:53-60.
[96] J. Hong, K. Kandasamy, M. Marimuthu, C. S. Choi, S. Kim. Electrical cell-substrate impedance sensing as a non-invasive tool for cancer cell study. Analyst. 2011;136:237-45.
[97] L. J. Yang, L. R. Arias, T. S. Lane, M. D. Yancey, J. Mamouni. Real-time electrical impedance-based measurement to distinguish oral cancer cells and non-cancer oral epithelial cells. Anal Bioanal Chem. 2011;399:1823-33.
[98] C. Murdoch, B. H. Brown, V. Hearnden, P. M. Speight, K. DApice, A. M. Hegarty, et al. Use of electrical impedance spectroscopy to detect malignant and potentially malignant oral lesions. Int J Nanomedicine. 2014;9:4521.
[99] Q. J. Liu, J. J. Yu, L. Xiao, J. C. O. Tang, Y. Zhang, P. Wang, et al. Impedance studies of bio-behavior and chemosensitivity of cancer cells by micro-electrode arrays. Biosens Bioelectron. 2009;24:1305-10.
[100] L. R. Arias, C. A. Perry, L. J. Yang. Real-time electrical impedance detection of cellular activities of oral cancer cells. Biosens Bioelectron. 2010;25:2225-31.
[101] A. Han, L. Yang, A. B. Frazier. Quantification of the Heterogeneity in Breast Cancer Cell Lines Using Whole-Cell Impedance Spectroscopy. Clin Cancer Res. 2007;13:139-43
[102] G. F. Qiao, W. Wang, W. Duan, F. Zheng, A. J. Sinclair, C. R. Chatwin. Bioimpedance Analysis for the Characterization of Breast Cancer Cells in Suspension. IEEE Trans Biomed Eng. 2012;59:2321-9.

[103] J. L. Hong, K. C. Lan, L. S. Jang. Electrical characteristics analysis of various cancer cells using a microfluidic device based on single-cell impedance measurement. Sensors Actuators B-Chem. 2012;173:927-34.
[104] V. Srinivasaraghavan, J. Strobl, M. Agah. Bioimpedance rise in response to histone deacetylase inhibitor is a marker of mammary cancer cells within a mixed culture of normal breast cells. Lab Chip. 2012;12:5168-79.
[105] V. Srinivasaraghavan, J. Strobl, D. Wang, J. R. Heflin, M. Agah. A comparative study of nano-scale coatings on gold electrodes for bioimpedance studies of breast cancer cells. Biomed Microdevices. 2014;16:689-96.
[106] V. Srinivasaraghavan, J. Strobl, M. Agah. Microelectrode bioimpedance analysis distinguishes basal and claudin-low subtypes of triple negative breast cancer cells. Biomed Microdevices. 2015;17:80.
[107] M. As. Mansor, M. R. Ahmad. Single Cell Electrical Characterization Techniques. Int J Mol Sci. 2015;16:12686-712.
[108] X. Li, K. G. Klemic, M .A. Reed, F. J. Sigworth. Microfluidic System for Planar Patch Clamp Electrode Arrays. Nano Lett. 2006;6:815-9.
[109] G. Mernier, E. Duqi, P. Renaud. Characterization of a novel impedance cytometer design and its integration with lateral focusing by dielectrophoresis. Lab Chip. 2012;12:4344-9.
[110] S. I. Han, Y. D. Joo, K. H. Han. An electrorotation technique for measuring the dielectric properties of cells with simultaneous use of negative quadrupolar dielectrophoresis and electrorotation. Analyst. 2013;138:1529-37.
[111] Y. Cho, H. S. Kim, A. B. Frazier, Z. G. Chen, D. M. Shin, A. Han. Whole-Cell Impedance Analysis for Highly and Poorly Metastatic Cancer Cells. J Microelectromech Syst. 2009;18:808-17.
[112] V. Srinivasaraghavan, D. Aggarwal, H. Babahosseini, D. Nakidde, J. Strobl, M. Agah. Analyses of single-cell mechanoelectrical properties via microfluidics. IEEE Sensors. Valencia, SpainNovember 2014. p. 1772 - 5.
[113] C. R. Gault, L. M. Obeid, Y. A. Hannun. An overview of sphingolipid metabolism: from synthesis to breakdown. Adv Exp Med Biol. 2010;688:1-23.
[114] B. Ogretmen, Y.A. Hannun. Biologically active sphingolipids in cancer pathogenesis and treatment. Nat Rev Cancer. 2004;4:604-16.
[115] N. N. Patwardhan, E. A. Morris, M. R. Raje, M. Gao, Y. Kharel, J. L. Tomsig, et al. Structure−Activity Relationship Studies and in Vivo Activity of Guanidine-Based Sphingosine Kinase Inhibitors: Discovery of SphK1- and SphK2-Selective Inhibitors. J Med Chem. 2015;58:1879-99.
[116] Knott K, Kharel Y, Raje MR, Lynch KR, Santos WL. Effect of alkyl chain length on sphingosine kinase 2 selectivity. Bioorg Med Chem Lett. 2012;22:6817-20.
[117] Raje MR, Knott K, Kharel Y, Bissel P, Lynch KR, Santos WL. Design, synthesis and biological activity of sphingosine kinase 2 selective inhibitors. Bioorg Med Chem Lett. 2012;20:183-94.
[118] Y. Zhao, X. Zhao, D. Chen, Y. Luo, M. Jiang, C. Wei, et al. Tumor cell characterization and classification based on cellular specific membrane capacitance and cytoplasm conductivity. Biosensors and Bioelectronics. 2014;57:245–53.

[119] B. Szachowicz-Petelska, I. Dobrzynska, S. Sulkowski, Z. Figaszewski. Characterization of the cell membrane during cancer transformation. Journal of Environmental Biology. 2010;31:845-50.
[120] M. L. Doria, C. Z.Cotrim, C. Simoes, B. Macedo, P. Domingues, M. R. Domingues, et al. Lipidomic Analysis of Phospholipids From Human Mammary Epithelial and Breast Cancer Cell Lines. J Cell Physiol. 2013;228:457-68.
[121] X. Liang, K. A. Graham, A. C. Johannessen, D. E. Costea, F. H. Labeed. Human oral cancer cells with increasing tumorigenic abilities exhibit higher effective membrane capacitance. Integr Biol. 2014;6:545-54.
[122] H. J. Mulhall, F. H. Labeed, B. Kazmi, D. E. Costea, M. P. Hughes, M. P. Lewis. Cancer, pre-cancer and normal oral cells distinguished by dielectrophoresis. Anal Bioanal Chem. 2011;401:2455-63.
[123] A. Salmanzadeh, E. S. Elvington, P. C. Roberts, E. M. Schmelz, R. V. Davalos. Sphingolipid metabolites modulate dielectric characteristics of cells in a mouse ovarian cancer progression model. Integr Biol. 2013;5:843-52.
[124] H. W. Hou, Q. S. Li, G. Y. H. Lee, A. P. Kumar, Ong CN, C. T. Lim. Deformability study of breast cancer cells using microfluidics. Biomed Microdevices. 2009;11:557-64.
[125] H. Babahosseini, V. Srinivasaraghavan, M. Agah. Microfluidic Chip Bio-Sensor for Detection of Cancer Cells. IEEE Sensors. Taipei, TaiwanOctober 2012. p. 1-4.
[126] E. H. Zhou, R. Krishnan, W. D. Stamer, K. M. Perkumas, K. Rajendran, J. F. Nabhan, et al. Mechanical responsiveness of the endothelial cell of Schlemm's canal: scope, variability and its potential role in controlling aqueous humour outflow. J R Soc Interface. 2012;9:1144-55.
[127] F. T. Arce, J. L. Whitlock, A. A. Birukova, K. G. Birukov, M. F. Arnsdorf, R. Lal, et al. Regulation of the Micromechanical Properties of Pulmonary Endothelium by S1P and Thrombin: Role of Cortactin. Biophys J. 2008;95:886–94.

Appendix A: MATLAB Codes

Matlab code used to extract entry and travel times in addition to the impedance magnitude and phase angels of individual cells in four frequencies from the impedance measurements:

```
clear;
clc;
%Enter cell number in Line 4
j=1;
in_path='C:\Users\Desktop\Run1 Demod0.xls';
in_path1='C:\Users\Desktop\Run1 Demod1.xls';
in_path2='C:\Users\Desktop\Run1 Demod2.xls';
in_path3='C:\Users\Desktop\Run1 Demod3.xls';
out_path='C:\Users\Desktop\Run1\DataAnalysis.xls';

if(j==1)
    f=fopen(char(out_path),'a+');

    fprintf(f,'%s\t%s\t%s\t%s\t%s\t%s\t%s\t%s\t%s\t%s\t%s\t%s\t%s\t%s\t%s\t%
    s\t%s\t%s\t%s\t%s\t%s\t%s\n','Cell Number','T entry','T in','T
    middle','T exit','Z baseline@1MHz','Z peak@1MHz','Theta
    baseline@1MHz','Theta peak@1MHz','Z baseline@100k','Z
    peak@100k','Theta baseline@100k','Theta peak@100k','Z
    baseline@10k','Z peak@10k','Theta baseline@10k','Theta peak@10k','Z
    baseline@1k','Z peak@1k','Theta baseline@1k','Theta peak@1k');
    fclose(f);
end

data=dlmread(in_path,'\t');
data1=dlmread(in_path1,'\t');
data2=dlmread(in_path2,'\t');
data3=dlmread(in_path3,'\t');
Z_mag=data(:,1);
Z_phase=data(:,2);
t=data(:,6);
Z_mag1=data1(:,1);
Z_phase1=data1(:,2);
t1=data1(:,6);
Z_mag2=data2(:,1);
Z_phase2=data2(:,2);
t5=data2(:,6);
Z_mag3=data3(:,1);
Z_phase3=data3(:,2);
t3=data3(:,6);
figure(1);
plot(t,Z_mag);
disp('Please select lower left and upper right corners of boxes (in that
order)');
disp('for all cells you wish to analyze and then press enter');
[x,y]=ginput;

for i=1:2:numel(x)
    clc;
```

```
if(i>1)
    clear X;
    clear Y;
end
figure(2);
h1=subplot(1,1,1);
plot(t,Z_mag);
set(h1,'XLim',[x(i) x(i+1)]);
clc;
disp('Please select 5 points on Figure 2 (top left) corresponding to
times where');
disp('1. Cell starts deformation to enter channel');
disp('2. Cell completely enters channel');
disp('3. Cell is in middle of channel');
disp('4. Cell completely exits channel');
disp('5. No cell');
disp('Next select two points corresponding to baseline and peak
values in all other plots');
disp('and then press enter');
[X,Y]=ginput;
f=fopen(char(out_path),'a+');
fprintf(f,'%s\t',char(strcat('Cell',int2str(j))));

for p=1:1:length(t)
    if t(p)>X(5);
        i_b=p-1;
        break;
    end
end

Y(6)=-180-Z_phase(i_b);
Y(8)=Z_mag1(i_b);
Y(10)=-180-Z_phase1(i_b);
Y(12)=Z_mag2(i_b);
Y(14)=-180-Z_phase2(i_b);
Y(16)=Z_mag3(i_b);
Y(18)=-180-Z_phase3(i_b);

for k=1:1:length(t)
    if t(k)>X(3);
        i_c=k-1;
        break;
    end
end

Y(7)=-180-Z_phase(i_c);
Y(9)=Z_mag1(i_c);
Y(11)=-180-Z_phase1(i_c);
Y(13)=Z_mag2(i_c);
Y(15)=-180-Z_phase2(i_c);
Y(17)=Z_mag3(i_c);
Y(19)=-180-Z_phase3(i_c);

fprintf(f,'%6.4f\t%6.4f\t%6.4f\t%6.4f\t%10f\t%10f\t%2.2f\t%2.2f\t%10
f\t%10f\t%2.2f\t%2.2f\t%10f\t%10f\t%2.2f\t%2.2f\t%10f\t%10f\t%2.2f\t
```

```
    %2.2f\n',[X(1) X(2) X(3) X(4) Y(5) Y(3) Y(6) Y(7) Y(8) Y(9) Y(10)
    Y(11) Y(12) Y(13) Y(14) Y(15) Y(16) Y(17) Y(18) Y(19)]);
    fclose(f);
    j=j+1;
end
```

Matlab code used to extract individual cell bioelectrical parameters from the impedance magnitudes and phase angles in four frequencies:

```
clear;
clc;
%Read Experimental Values
fn1='C:\Users\Desktop\DataAnalysis.xls';
rD=xlsread(fn1);
out_path='C:\Users\Desktop\DataAnalysis_Parameters.xls';

file=fopen(char(out_path),'a+');
fprintf(file,'%s\t%s\t%s\t%s\t%s\t%s\t%s\t\t%s\t%s\t%s\t%s\t%s\n','Cell
Number','Qdl','ndl','Rsp','Qpar','npar','RsquareBaseline','Rint','Qm','n
m','Rcyt','RsquarePeak');
fclose(file);

%List of frequencies used
freq=[1e3; 1e4;  1e5; 1e6];

%Extract baseline and peak values of impedance
k=1;
for i=1:1:size(rD,1)
    for j=5:4:size(rD,2)
        Zb_mag(i,k)=rD(i,j);
        Zp_mag(i,k)=rD(i,j+1);
        k=k+1;
    end
    k=1;
end

for i=1:1:size(rD,1)

    % curve fitting for Baseline
    Zb=transpose(Zb_mag(i,:));
    ftype_baseline=fittype('abs((((j*Cdl*2*pi*f)^-ndl+Rsp*1e12)^-
    1+(j*4.185e-14*2*pi*f)^0.845)^-1)','independent',
    {'f'},'dependent',{'Zb'},'coefficients',{'Cdl','ndl','Rsp'});

    foptions_baseline=fitoptions('Method','NonlinearLeastSquares','Algor
    ithm','Trust-Region','DiffMaxChange', 1e-15,'DiffMinChange',1e-
    15,'MaxFunEvals',2e3,'MaxIter',2e3,'TolX',1e-15,'TolFun',1e-
    15,'Lower',[1e-14,0.6,6e-7],'Upper',[1e-13,1,5e-6],'Startpoint',[1e-
    14,0.1,1e-6]);
    [fobjb gofb]=fit(freq,Zb,ftype_baseline,foptions_baseline);
    Cdl(i)=fobjb.Cdl;
    ndl(i)=fobjb.ndl;
    Rsp(i)=fobjb.Rsp*1e12;
    Cpar(i)=4.185e-14;
    npar(i)=0.845;
```

```
    Rsquareb(i)=gofb.adjrsquare;

    % curve fitting for Peak
    Zp=transpose(Zp_mag(i,:));
    ftype_peak=fittype('abs((((j*Cdl*2*pi*f)^-ndl+0.7*Rsp+((Rint*1e12)^-
    1+((j*2*pi*f*Cm)^-nm+Rcyt*1e12)^-1)^-1)^-1+(j*4.185e-
    14*2*pi*f)^0.845)^-1)','problem',{'Cdl','ndl','Rsp'},'independent',
    {'f'},'dependent',{'Zp'},'coefficients',{'Rint','Cm','nm','Rcyt'});

    foptions_peak=fitoptions('Method','NonlinearLeastSquares','Algorithm
    ','Trust-Region','DiffMaxChange', 1e-15,'DiffMinChange',1e-
    15,'MaxFunEvals',2e3,'MaxIter',2e3,'TolX',1e-15,'TolFun',1e-
    15,'Lower',[9e-8,1e-14,0.7,4e-8],'Upper',[2e-6,1e-13,1,4.75e-
    7],'Startpoint',[1e-6,1e-14,0.1,1e-7]);
    [fobjp gofp]=fit(freq,Zp,ftype_peak,foptions_peak,'problem',{Cdl(i),
    ndl(i), Rsp(i)});
    Rint(i)=fobjp.Rint*1e12;
    Cm(i)=fobjp.Cm;
    nm(i)=fobjp.nm;
    Rcyt(i)=fobjp.Rcyt*1e12;
    Rsquarep(i)=gofp.adjrsquare;

    %Print Values in Spreadsheet
    file=fopen(char(out_path),'a+');
    fprintf(file,'%u\t%e\t%e\t%e\t%e\t%e\t%e\t\t%e\t%e\t%e\t%e\t%e\n',[i
    Cdl(i) ndl(i) Rsp(i) Cpar(i) npar(i) Rsquareb(i) Rint(i) Cm(i) nm(i)
    Rcyt(i) Rsquarep(i)]);
    fclose(file);
end
```